5. Tao, Y. *et al.* Assembly of a tailed bacterial virus and its genome release studied in three dimensions. *Cell* **95,** 431–437 (1998).
6. Valpuesta, J. M. & Carrascosa, J. L. Structure of viral connectors and their function in bacteriophage assembly and DNA packaging. *Q. Rev. Biophys.* **27,** 107–155 (1994).
7. Guo, P., Erickson, S. & Anderson, D. A small viral RNA is required for in vitro packaging of bacteriophage ϕ29 DNA. *Science* **236,** 690–694 (1987).
8. Zhang, F. *et al.* Function of hexameric RNA in packaging of bacteriophage ϕ29 DNA *in vitro*. *Mol. Cell* **2,** 141–147 (1998).
9. Guo, P., Zhang, C., Chen, C., Garver, K. & Trottier, M. Inter-RNA interaction of phage ϕ29 pRNA to form a hexameric complex for viral DNA transportation. *Mol. Cell* **2,** 149–155 (1998).
10. Müller, D. J., Engel, A., Carrascosa, J. L. & Vélez, M. The bacteriophage ϕ29 head-tail connector imaged at high resolution with the atomic force microscope in buffer solution. *EMBO J.* **16,** 2547–2553 (1997).
11. Valpuesta, J. M., Fernández, J. J., Carazo, J. M. & Carrascosa, J. L. The three-dimensional structure of a DNA translocating machine at 10 Å resolution. *Structure* **7,** 289–296 (1999).
12. Valle, M. *et al.* Domain architecture of the bacteriophage ϕ29 connector protein. *J. Mol. Biol.* **288,** 899–909 (1999).
13. Guasch, A. *et al.* Crystallographic analysis reveals the 12-fold symmetry of the bacteriophage ϕ29 connector particle. *J. Mol. Biol.* **281,** 219–225 (1998).
14. Badasso, M. O. *et al.* Purification, crystallization, and initial X-ray analysis of the head-tail connector of bacteriophage ϕ29. *Acta Crystallogr. D* **56,** 1187–1190 (2000).
15. Vlcek, C. & Paces, V. Nucleotide sequence of the late region of *Bacillus* ϕ29 completes the 19285-bp sequence of ϕ29 genome. Comparison with the homologous sequence of phage PZA. *Gene* **46,** 215–225 (1986).
16. Grimes, S. & Anderson, D. RNA dependence of the bacteriophage ϕ29 DNA packaging ATPase. *J. Mol. Biol.* **215,** 559–566 (1990).
17. Donate, L. E., Valpuesta, J. M., Mier, C., Rojo, F. & Carrascosa, J. L. Characterization of an RNA-binding domain in the bacteriophage ϕ29 connector. *J. Biol. Chem.* **268,** 20198–20204 (1993).
18. Reinisch, K. M., Nibert, M. L. & Harrison, S. C. Structure of the reovirus core at 3.6 Å resolution. *Nature* **404,** 960–967 (2000).
19. Ibarra, B. *et al.* Topology of the components of the DNA packaging machinery in the phage ϕ29 prohead. *J. Mol. Biol.* **298,** 807–815 (2000).
20. Guo, P., Peterson, C. & Anderson, D. Prohead and DNA-gp3-dependent ATPase activity of the DNA packaging protein gp16 of bacteriophage ϕ29. *J. Mol. Biol.* **197,** 229–236 (1987).
21. Dube, P., Tavares, P., Lurz, R. & van Heel, M. The portal protein of bacteriophage SPP1: a DNA pump with 13-fold symmetry. *EMBO J.* **12,** 1303–1309 (1993).
22. Abrahams, J. P., Leslie, A. G. W., Lutter, R. & Walker, J. E. Structure at 2.8 Å resolution of F_1-ATPase from bovine heart mitochondria. *Nature* **370,** 621–628 (1994).
23. Silverman, M. R. & Simon, M. I. Flagellar rotation and the mechanism of bacterial motility. *Nature* **249,** 73–74 (1974).
24. Vale, R. D. & Milligan, R. A. The way things move: looking under the hood of molecular motor proteins. *Science* **288,** 88–95 (2000).
25. Rossmann, M. G. & Arnold, E. *International Table for Crystallography* Vol. F (International Union of Crystallography, Kluwer Academic, Dordrecht) (in the press).
26. Baker, T. S. & Cheng, R. H. A model-based approach for determining orientations of biological macromolecules imaged by cryoelectron microscopy. *J. Struct. Biol.* **116,** 120–130 (1996).
27. Bailey, S. *et al.* Phylogenetic analysis and secondary structure of the *Bacillus subtilis* bacteriophage RNA required for DNA packaging. *J. Biol. Chem.* **265,** 22365–22370 (1990).
28. Reid, R. J. D., Bodley, J. W. & Anderson, D. Identification of bacteriophage ϕ29 prohead RNA domains necessary for *in vitro* DNA-gp3 packaging. *J. Biol. Chem.* **269,** 9084–9089 (1994).

Acknowledgements

We thank J. Carrascosa for comments and discussions of this paper. We also thank the staff of CHESS, APS BioCARS and APS Structural Biology Center for assistance in data collection. This work was supported by the NSF (M.G.R.), the NIH (D.L.A. and T.S.B.), and an NSF Shared Instrumentation grant (T.S.B. and M.G.R).

Correspondence and requests for materials should be addressed to M.G.R. (e-mail: mgr@indiana.bio.purdue.edu). Coordinates of the connector (accession number 1FOU) and pRNA (accession number 1FOQ) have been deposited with the Protein Data Bank.

errata

Logical computation using algorithmic self-assembly of DNA triple-crossover molecules

Chengde Mao, Thomas H. LaBean, John H. Reif & Nadrian Seeman

Nature **407,** 493–496 (2000).

In Fig. 2 of this paper, y_2 should have equalled 0 in Calculation 1; and x_2, y_3 and y_4 should have equalled 0 in Calculation 2. □

Acceleration of global warming due to carbon-cycle feedbacks in a coupled climate model

Peter M. Cox, Richard A. Betts, Chris D. Jones, Steven A. Spall & Ian J. Totterdell

Nature **408,** 184–187 (2000).

In this paper, part of the labelling of Figs 2–4 was printed incorrectly. In Fig. 2, the year 2950 should have been 2050. In Figs 2 and 3, the year 1050 should have been 1950. In Fig. 4, the numbers on the *y* axis should have been labelled sequentially from −200 to +400; in addition, in Fig. 4a the *y* axis should have been labelled 'Changes in vegetation carbon (Gt C)'. □

correction

Allometric scaling of production and life-history variation in vascular plants

Brian J. Enquist, Geoffrey B. West, Eric L. Charnov & James H. Brown

Nature **401,** 907–911 (1999).

In the last sentence of the abstract the relative growth rate equation, presented as $(1/M)\,(\mathrm{d}M/\mathrm{d}f)$, should read $(1/M)\,(\mathrm{d}M/\mathrm{d}t)$. Also, the sentence following that containing equation (5) should read "Thus, regardless of any possible time dependence of either the proportionality constants or the density, a plot of $M^{1/4}$ versus $M_0^{1/4}$ for fixed times t and t_0 for any species should yield a straight line with a universal slope of unity but with an intercept that depends on the time interval and the species."

In other words, the primary relationship is in terms of mass, M and not diameter, D. Equations (4) and (5), which relate the dependence of trunk diameter, D, on time, t, are only valid if the proportionality constant $A \equiv C_D/\rho^{3/8}$ is time-independent; A is the proportionality constant in the allometric relation $D = AM^{3/8}$ of equation (3). This is needed because data are typically given in terms of D rather than M. The other proportionality constants, C_G and C_B, occurring, respectively, in the growth equation (2) and allometric equation for metabolic rate (3), can be time-dependent.

As our analysis of the data assumed time-independence of all of these coefficients as well as of wood density, ρ (see below equation (6)), this oversight does not affect our results or conclusions. If A were slowly varying, it would contribute a small correction to the unit slope prediction given by $(t - t_0)d$, where d is the logarithmic derivative of A. This is expected to be very small, especially as the time interval $(t - t_0)$ is small relative to the lifespan of the species sampled. Furthermore, any time dependence in A is almost certainly smaller than its variation across species and effects arising from neglecting maintenance costs in the growth equation (2). We thank J. Banavar, J. Damuth, A. Maritan and A. Rinaldo for bringing this oversight to our attention. □

excited a second time, all within 35 ps. We have estimated the value of $p(2)$ and find it to be less than 8×10^{-4} at our maximum intensity.

To directly demonstrate the non-classical sub-poissonian statistics of our source, we measured the intensity correlation function of the emitted light with the coincidence set-up of Fig. 1d. For both the single-molecule (Fig. 4a) and background (Fig. 4b) cases, the histograms show the expected peak pattern, given the time pattern of the photon emission in the inset of Fig. 2. For poissonian light, such as that from an attenuated pulsed laser or the fluorescence from the background excited by the laser pulses, the central peak is identical in intensity and shape to the lateral ones (Fig. 4b). In the case of a single molecule, the central peak should vanish altogether as no more than one single photon can be emitted by the molecule. The ratio of the central peak's area to the area of the lateral peaks is the signature of the sub-poissonian statistics of the light emitted by our source. The residual peak at zero delay in Fig. 4a arises from coincidence events involving background photons excited during each laser pulse. In our experiment, the background signal shows a lifetime of about 4 ns, which indicates that it arises from weak fluorescence from out-of-focus terrylene molecules, not from Raman scattering.

It is convenient to compare the probability distribution $p(m)$ for our source to that expected from a Poisson distribution by means of the Mandel parameter $Q_s = (\sigma^2 - n_{av})/n_{av}$, where σ^2 is the variance of the distribution and n_{av} is the average number of photons[26]. At the highest pumping power, the probabilities of our source are $p(0) = 0.14$, $p(1) = 0.86$ and $p(m > 1) \approx 0$. This distribution is radically different from that for a pulsed coherent source with the same $n_{av} = 0.86$: $p_{coh}(0) = 0.42$, $p_{coh}(1) = 0.36$, $p_{coh}(2) = 0.16$, ... The Mandel parameter of our source is $Q_s = -0.86$, not far from -1, the value expected for a perfect single-photon emitter, and far from 0, the value for a poissonian source. The Mandel parameter Q_d of the detected photon counts is naturally affected by the light detection efficiency[27]. Using $Q_d = Q_s(\eta/2)$, we find $Q_d \approx -3\%$.

The parameters of our source (repetition rate and single-photon generation probability) are limited only by the laser system used; nevertheless, the current performance already surpasses that of previous work. This high performance combined with the simplicity of our source may make it suitable for a variety of quantum optical experiments and for other applications where triggered single photons are needed. Photons are emitted into a range of solid angles, which can limit the detection efficiency; however, optical solutions to this problem can be envisaged, that is, one can imagine that the single molecule could be coupled to a single cavity mode to reduce losses, change the emission pattern, or modify the emission lifetime and thus increase the emission rate. To reduce the background (from out-of-focus molecules or Raman scattering), reduced terrylene doping, pumping with z-axis polarized light, or use of a crystalline system with a more favourable orientation of the single absorber can be utilized. With further development, single molecules in solids may soon provide compact and reliable sources of single photons. □

Received 27 January; accepted 15 August 2000.

1. Meystre, P. & Sargent, M. III *Elements of Quantum Optics* (Springer, Berlin, 1991).
2. Drummond, P. D. *Quantum Squeezing* (Springer, Berlin, 1999).
3. Special issue on quantum information. *Phys. World* **11**(3), (1998).
4. Bennett, C. H., Brassard, G. & Ekert, A. K. Quantum cryptography. *Sci. Am.* **267**(4), 50–57 (1992).
5. Turchette, Q. A., Hood, C. J., Lange, W., Mabuchi, H. & Kimble, H. J. Measurement of conditional phase shifts for quantum logic. *Phys. Rev. Lett.* **75,** 4710–4713 (1995).
6. Parkins, A. S., Marte, P., Zoller, P., Carnal, O. & Kimble, H. J. Quantum-state mapping between multilevel atoms and cavity light fields. *Phys. Rev. A* **51,** 1578–1596 (1995).
7. Cirac, J. I., Zoller, P., Kimble, H. J. & Mabuchi, H. Quantum state transfer and entanglement distribution among distant nodes in a quantum network. *Phys. Rev. Lett.* **78,** 3221–3224 (1997).
8. Kuhn, A., Hennrich, M., Bondo, T. & Rempe, G. Controlled generation of single photons from a strongly coupled atom-cavity system. *Appl. Phys. B* **69,** 373–377 (1999).
9. Imamoglu, A., Schmidt, H., Woods, G. & Deutsch, M. Strongly interacting photons in a nonlinear cavity. *Phys. Rev. Lett.* **79,** 1467–1470 (1997).
10. Imamoglu, A. & Yamamoto, Y. Turnstile device for heralded single photons: coulomb blockade of electron and hole tunneling in quantum confined p-i-n heterojunctions. *Phys. Rev. Lett.* **72,** 210–213 (1994).
11. Kim, J., Benson, O., Kan, H. & Yamamoto, Y. A Single-photon turnstile device. *Nature* **397,** 500–503 (1999).
12. Brunel, C., Lounis, B., Tamarat, P. & Orrit, M. Triggered source of single photons based on controlled single molecule fluorescence. *Phys. Rev. Lett.* **83,** 2722–2725 (1999).
13. Xie, X. S. & Trautman, J. K. Optical studies of single molecules at room temperature. *Annu. Rev. Phys. Chem.* **49,** 441–480 (1998).
14. Moerner, W. E. & Orrit, M. Illuminating single molecules in condensed matter. *Science* **283,** 1670–1676 (1999).
15. Ambrose, W. P., Goodwin, P. M., Martin, J. C. & Keller, R. A. Single-molecule detection and photochemistry on a surface using near-field optical-excitation. *Phys. Rev. Lett.* **72,** 160–163 (1994).
16. Ambrose, W. P. *et al.* Fluorescence photon antibunching from single molecules on a surface. *Chem. Phys. Lett.* **269,** 365–370 (1997).
17. De Martini, F., Di Giuseppe, G. & Marrocco, M. *Phys. Rev. Lett.* **76,** 900–903 (1996).
18. Kiston, S. C., Jonsson, P., Rarity, J. G. & Tapster, P. R. Intensity fluctuation spectroscopy of small numbers of dye molecules in a microcavity. *Phys. Rev. A* **58,** 620–627 (1998).
19. Fleury, L., Sick, B., Zumofen, G., Hecht, B. & Wild, U. P. High photo-stability of single molecules in an organic crystal at room temperature observed by scanning confocal optical microscopy. *Mol. Phys.* **95,** 1333–1338 (1998).
20. Kulzer, F., Koberling, F., Christ, T., Mews, A. & Basche, T. Terrylene in p-terphenyl: single molecule experiments at room temperature. *Chem. Phys.* **247,** 23–34 (1999).
21. Basché, T., Moerner, W. E., Orrit, M. & Talon, H. Photon antibunching in the fluorescence of a single dye molecule trapped in a solid. *Phys. Rev. Lett.* **69,** 1516–1519 (1992).
22. Fleury, L., Segura, J.-M., Zumofen, G., Hecht, B. & Wild, U. P. Nonclassical photon statistics in single molecule fluorescence at room temperature. *Phys. Rev. Lett.* **84,** 1148–1151 (2000).
23. Kummer, S., Basché, T. & Bräuchle, C. Terrylene in p-terphenyl: a novel single crystalline system for single molecule spectroscopy at low temperatures. *Chem. Phys. Lett.* **229,** 309–316 (1994).
24. Plakhotnik, T., Moerner, W. E., Palm, V. & Wild, U. P. Single molecule spectroscopy: maximum emission rate and saturation intensity. *Opt. Commun.* **114,** 83–88 (1995).
25. Buttler, W. T. *et al.* Quantum key distribution over 1 km. *Phys. Rev. Lett.* **81,** 3283–3286 (1998).
26. Short, H. & Mandel, L. Observation of sub-poissonian photon statistics. *Phys. Rev. Lett.* **51,** 384–387 (1983).
27. Mandel, L. Sub-poissonian photon statistics in resonance fluorescence. *Opt. Lett.* **4,** 205–207 (1979).
28. Miller, G. D. *et al.* 42%-efficient single-pass cw second-harmonic generation in periodically poled lithium niobate. *Opt. Lett.* **22,** 1834–1836 (1997).

Acknowledgements

We thank Lightwave Electronics for use of the mode-locked Nd-YAG laser, M. Fejer and M. Fayer for providing non-linear crystals, and the Stanford Synchrotron Radiation Laboratory for providing the pulse height analyser. B. L. thanks D. Wright for assistance and NATO for Fellowship support.

Correspondence and requests for materials should be addressed to W.E.M. (e-mail: moerner@stanford.edu).

Logical computation using algorithmic self-assembly of DNA triple-crossover molecules

Chengde Mao*, Thomas H. LaBean†, John H. Reif† & Nadrian C. Seeman *

** Department of Chemistry, New York University, New York, 10003, USA & †Department of Computer Science, Duke University, Durham, North Carolina 27707, USA*

Recent work[1–3] has demonstrated the self-assembly of designed periodic two-dimensional arrays composed of DNA tiles, in which the intermolecular contacts are directed by 'sticky' ends. In a mathematical context, aperiodic mosaics may be formed by the self-assembly of 'Wang' tiles[4], a process that emulates the operation of a Turing machine. Macroscopic self-assembly has been used to perform computations[5]; there is also a logical equivalence between DNA sticky ends and Wang tile edges[6,7]. This suggests that the self-assembly of DNA-based tiles could be used to perform DNA-based computation[8]. Algorithmic aperiodic self-assembly requires greater fidelity than periodic self-assembly,

because correct tiles must compete with partially correct tiles. Here we report a one-dimensional algorithmic self-assembly of DNA triple-crossover molecules[9] that can be used to execute four steps of a logical (cumulative XOR) operation on a string of binary bits.

A variety of different DNA tile types have been used in previous assemblies, including double-crossover molecules[1], triple-crossover molecules[9], and parallelograms produced from Holliday junction analogues[3]. Here we have used triple-crossover molecules; their molecular structure is illustrated in Fig. 1a. The molecule contains four strands (shown in red, green, blue and purple) that self-assemble through Watson–Crick base pairing to produce three double helices in a roughly planar arrangement; each double helix is connected to adjacent double helical domains at two points where their strands cross over between them. The ends of the central double helix are closed by hairpin loops, but the other helices can terminate in sticky ends containing information that directs the assembly of the tiles.

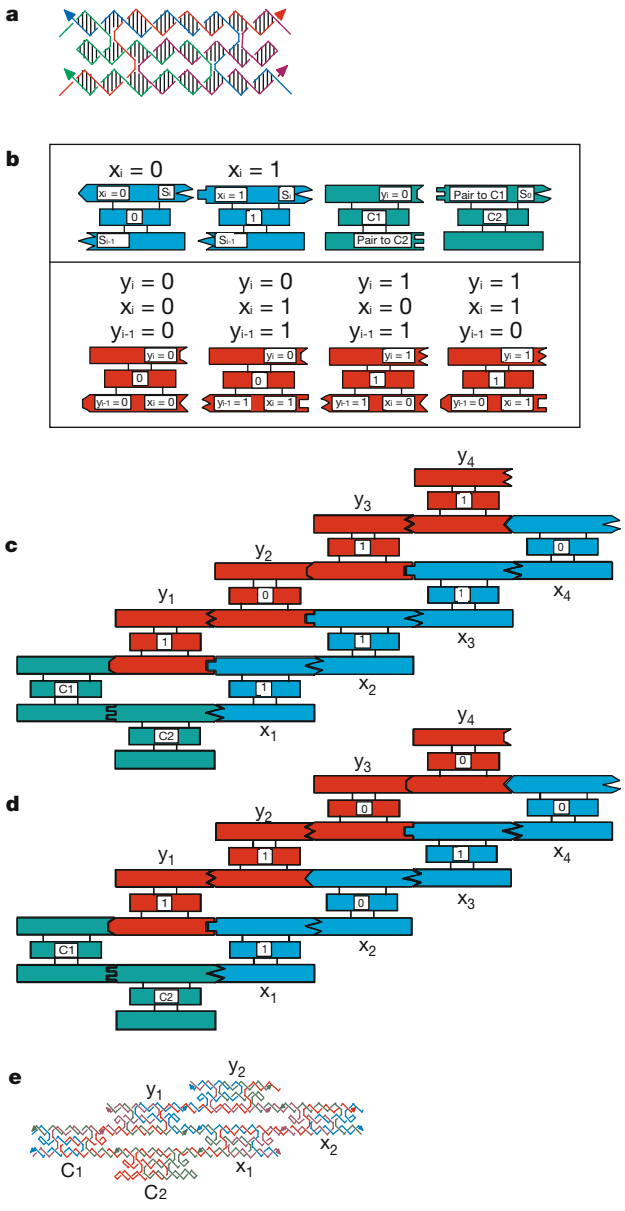

Figure 1 Calculation of cumulative XOR by self-assembly of DNA tiles. **a**, An individual triple-crossover tile. The four coloured backbone strands assemble to form three double-helical domains; arrowheads indicate 3′ ends. **b**, Component tiles. The three helical domains are drawn as rectangles, flanked by sticky ends shown as geometrical shapes. The value of each tile is in the central rectangle. The meaning of each sticky end is also indicated. Shown are the two x tiles (blue), the four y tiles (red), and the initialization corner tiles, C1 and C2 (green). The y_i tiles are upside down from the x_i tiles. **c**, **d**, The two calculations performed. The values of each tile are the same as in **b**, and the sticky ends are the same, although the labels have been omitted for clarity. The tiles are shown assembled to perform the cumulative XOR calculation; note the complementarity of sticky-ended association at each molecular interface. All sticky ends are asymmetric, so that when the same meanings touch (for example, $x_i = 0$ pairing with $x_i = 0$), the sequences are complementary, but not self-complementary. The operations are designed to proceed from lower left to upper right, because the x_i and C1 and C2 tiles have longer sticky ends than the y_i tiles. After the first y tile has been added, $x_1 = 1$ and $y_1 = 1$, for both arrays, because $y_1 = x_1$. In the next step, the array in **c** contains $x_2 = 1$: because $x_2 = y_1$, y_2 should be 0, and only the y tile with value 0 and inputs y_{i-1} and $x_i = 1$ fits properly between y_1 and x_2. In **d**, $x_2 = 0$, so $x_2 \neq y_1$, and y_2 should be 1, as shown. The sequences are available in the Supplementary Information. **e**, The reporter strand. At the end of the assembly, the reporter strand running through the x diagonal array, around the corner, and then back up the y diagonal array is ligated, thereby associating the calculated output with the input. The strand structure in the vicinity of the corner is shown, and the reporter strand is drawn with a thick red line.

In periodic assemblies, the sticky ends contain positional information that directs the associations of one or more tile types to produce a periodic lattice. Here, the sticky ends serve the same role, but the self-assembly of the tiles is used to perform a computation, and the arrangement of the tiles does not display simple periodicity. Figure 1b shows the tiles used to perform the cumulative XOR calculation. The tiles are represented schematically; the three helices are depicted as connected rectangular forms terminating in sticky ends, which are represented as geometrical shapes, or non-cohesive blunt ends and hairpins, which are drawn flush.

The result of the XOR operation is a 0 if two input numbers are the same (two zeros or two ones), but it is 1 if one of the two numbers is 0 and the other is 1. The cumulative XOR consists of a series of Boolean inputs x_1, x_2, x_3, ... x_n, and the output is also a series of Booleans, y_1, y_2, y_3, ... y_n, where $y_1 = x_1$, and for $i > 1$, $y_i = y_{i-1}\mathrm{XOR}x_i$. The value of any y_i in these calculations also reports the even or odd parity of the first i values of x. Thus, two different kinds of input x tiles are needed, one whose value is 0 and a second whose value is 1. Chemically, the value of a tile, 0 or 1, is denoted by the presence of a restriction site: Pvu II (CAGCTG) represents 0 and EcoR V (GATATC) represents 1.

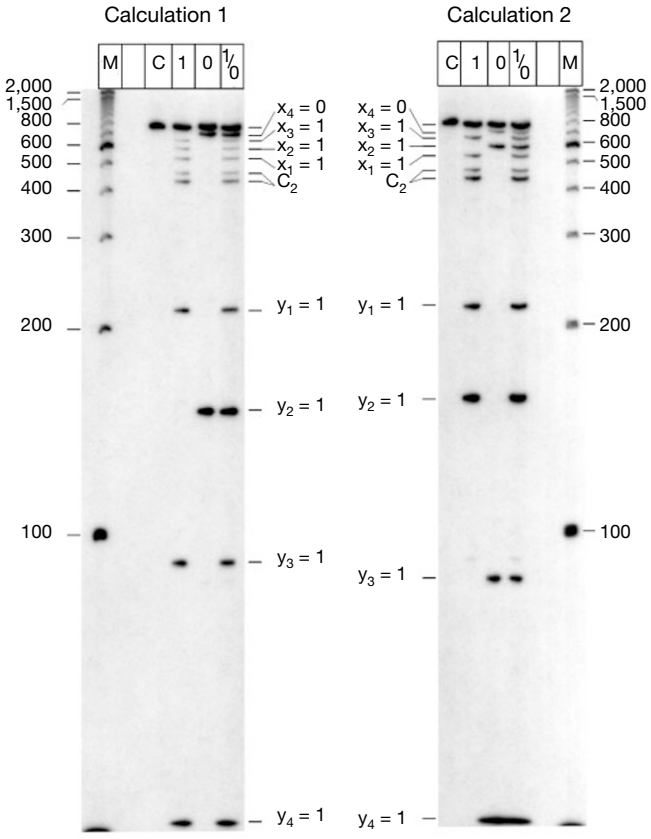

Figure 2 Denaturing gels illustrating cumulative XOR calculations. Two 6% denaturing gels are shown, corresponding to the two calculations described. M, lanes containing 100-mer marker ladders; C, lanes containing undigested reporter strands. The lanes digested with Pvu II are labelled 0, to indicate that sensitivity to this enzyme represents a tile with the value zero, and those digested with EcoR V are labelled 1, because the site for that enzyme represents a value of one. A lane combining the two individual digestions is labelled 1/0. The bands corresponding to the input values x_4, x_3, x_2 and x_1 are visible at the tops of the lanes, in descending order. The C2 tile contains a hairpin with an EcoR V site, so the site is present twice in the reporter strand at that location. The bands corresponding to the output values y_1, y_2, y_3 and y_4 are visible at the bottom of the gel. Faint bands corresponding to erroneous Pvu II cleavage are visible near y_2 in calculation 1 and y_3 in calculation 2. A faint band corresponding to erroneous EcoR V cleavage is present near y_3 in calculation 1.

The x tiles are shown in blue in Fig. 1b: Their value (0 or 1) is shown in their central rectangle, the upper-left sticky end reports this value, and the upper-right and lower-left sticky ends provide the means of connecting successive x tiles. These sticky ends are shown as geometrically complementary, as they would be for a general set of 16 parallel calculations. However, to demonstrate the efficacy of the procedure, the calculations performed here are definite four-bit calculations for which the order of the input x tiles was specified exactly by a series of different sticky ends.

Like x tiles, two values of y tiles are necessary, again representing 0 and 1. However, there are two ways to get each of these results: the value of a y tile can be 0 either because both inputs are 0 or because both are 1; likewise, the value of a y tile can be 1 because the value of one input is 0 and the other is 1, or vice versa. Thus, four different y tiles are needed.

The y tiles are shown in red in Fig. 1b. The tile values again are displayed on the central domain, and this value is reported by the sticky end on the right of the upper domain. The two inputs derive from the sticky ends on the left (y_{i-1}) and right (x_i) of the bottom domain. We note that the same sticky end in the input domain represents a given input, independent of the other end. For example, the right-side sticky end $x_i = 1$ has the same shape (sticky end) regardless of whether the left-side sticky end represents $y_{i-1} = 0$ (leading to a tile value of 1) or $y_{i-1} = 1$ (leading to a tile value of 0). There are only two different left sticky ends in the input (bottom) domain, and likewise only two different right sticky ends. Consequently, both sticky ends on each tile must pair correctly for the proper y_i tile to be inserted in the assembly. In contrast to periodic assembly, where correct tiles compete with incorrect tiles for each site in the lattice, here correct tiles are competing with partially correct tiles.

We have performed two different XOR-related self-assemblies, illustrated in Fig. 1c and d. In addition to the x and y tiles, two corner tiles, C1 and C2 (green in Fig. 1b) are used to initialize the two values of x_1 and y_1, and to connect the input to the output. The self-assembly in Fig. 1c has the inputs $x_1 = x_2 = x_3 = 1$ and $x_4 = 0$. These correspond to output values of $y_1 = 1$, $y_2 = 0$, and $y_3 = y_4 = 1$. In a second self-assembly (Fig. 1d), $x_1 = 1$, $x_2 = 0$, $x_3 = 1$ and $x_4 = 0$, corresponding to $y_1 = y_2 = 1$ and $y_3 = y_4 = 0$. Note that for $i > 1$, the sticky ends on the bottom domain of each y_i tile complement those on the y_{i-1} tile on its left and the x_i tile on its right.

Once the self-assembly has occurred, it is necessary to extract the answer. For this purpose, each molecular tile contains a 'reporter strand'[10], which traverses the tile in a diagonal pathway[9]; the reporter strand is illustrated as a thick red strand in the tile shown in Fig. 1a, which is an x-type tile. Following self-assembly, the reporter strands are ligated to each other to produce a long reporter strand that contains the inputs and outputs of the calculation. The ligated long reporter strand in the vicinity of the corner of the assembly is shown as a thick red strand on the molecular diagram in Fig. 1e.

The sticky ends used in the assembly of the C_1–C_2–x_1–x_2–x_3–x_4 unit contain seven nucleotides, and the sticky ends used to include the y_i tiles in the assembly contain five nucleotides. The tiles were first assembled individually from their component strands by cooling slowly from 90 °C to room temperature, as done previously[1–3]. 20-μl aliquots of stock solutions (in USB ligation buffer) of both C tiles (100 nM), the four x tiles (100 nM), and the four y tiles (400 nM) were then combined and incubated for 30 min each at temperatures of 37, then 22, and finally 4 °C. During incubation and subsequent steps, 20-μl aliquots of three double helices, each with a sticky end (one helix to pair with the free sticky end on x_4 and two helices to pair with the two possible free sticky ends on y_4), that contained radioactively labelled PCR primers (800 nM) were also present in solution.

Ligation was initiated by adding 20 units of T4 DNA ligase and,

over a 3-hour period, the solution was brought slowly to 16 °C as ligation proceeded. The strand was amplified by polymerase chain reaction (PCR), using the primers that were ligated to each end of the long reporter strand. A strand of the proper length was eluted from a denaturing gel, was re-annealed, and was subjected to restriction by either of the restriction enzymes. The results are displayed in Fig. 2. The answer produces a barcode display, much like that used in ref. 11 to visualize the answers to RNA computation of chess problems. The correct answers are evident as dark bands in the gels shown in Fig. 2.

Small proportions of incorrect bands are visible on the original gels for both calculations. Thus, in lane 1 (EcoR V) of calculation 1, there is an incorrect band at the 0 position of y_2, and a similar incorrect band in the 0 lane at y_3 is also present. However, if the array fills from the corner, some of the incorrect y_3 intensity could result from 'correct' molecules propagating the previous error. Similarly, calculation 2 has one detectable error band resulting from cleavage of EcoR V at y_3.

We estimate the error level to be about 2–5%, but quantitative error analysis is complicated by differential cleavage activities between the two enzymes, combined with the possibility of star-activity (sequence infidelity) and probable multiple cleavage of the same strand. Also, the individual enzymes cleave with different activities at different sites, as seen in the differential cleavage of the two EcoR V sites in the C2 tile. We may have reduced our observation of self-assembly errors by selecting only those tiles that ligated correctly, because the enzyme specificity for exact pairing, although imperfect[12], may have performed some discrimination for the system. A previous two-molecule, single-step competition experiment estimated error rates below 1.6% (ref. 13).

The algorithmic molecular assembly described here demonstrates a non-trivial DNA computation done by self-assembly. Examples of SAT (satisfaction) problems solved in a DNA context[11,14,15] entailed laboratory operations for each clause in a logical statement, whereas a single self-assembly step is used here. This suggests that computation by self-assembly may be scalable. Another recent work[16] also uses only a single assembly step, but its scalability relies on proper hairpin formation in very long single-stranded molecules.

XOR computation on pairs of bits (as done here) can be used for executing a one-time pad cryptosystem that provides theoretically unbreakable security[17]. Other applications could involve the algorithmically directed self-assembly of intricate patterns and smart materials. We used y tiles repetitively in both assemblies, and would need no more species of y tiles, regardless of the length of the calculation. Thus, if the assembly principles applied here can be extended to two and three dimensions, it will be possible to prepare nanoscale patterns and smart materials by laying out components algorithmically, without the need to specify and prepare a unique element for every position of the array.

By using more nucleotides in the sticky ends of the input tiles than the output tiles, we have used the principle of 'frames'[6,7,18] This feature performs the computation in the presence of a well-defined border. Such borders are likely to be useful, because they set limits on the extent of the calculation or patterning; combining framed arrays will facilitate a modular approach to the process. □

Received 27 April; accepted 3 August 2000.

1. Winfree, E., Liu, F., Wenzler, L. A. & Seeman, N. C. Design and self-assembly of two-dimensional DNA crystals. *Nature* **394,** 539–544 (1998).
2. Liu, F., Sha, R. & Seeman, N. C. Modifying the surface features of two-dimensional DNA crystals. *J. Am. Chem. Soc.* **121,** 917–922 (1999).
3. Mao, C., Sun, W. & Seeman N. C. Designed two-dimensional DNA Holliday junction arrays visualized by atomic force microscopy. *J. Am. Chem. Soc.* **121,** 5437–5443 (1999).
4. Wang, H. in *Proceedings of a Symposium in the Mathematical Theory of Automata* 23–26 (Polytechnic Press, New York, 1963).
5. Rothemund, P. W. K. Using lateral capillary forces to compute by self-assembly. *Proc. Nat. Acad. Sci. USA* **97,** 984–989 (2000).
6. Winfree, E. in *DNA Based Computers: Proceedings of a DIMACS Workshop, April 4, 1995, Princeton University* (eds Lipton, R. J. & Baum, E. B.) 199–221 (American Mathematical Society, Providence, RI, 1996).
7. Winfree, E. *Algorithmic Self-Assembly of DNA*. PhD Thesis, Caltech (1998).
8. Adleman, L. Molecular computation of solutions to combinatorial problems. *Science* **266,** 1021–1024 (1994).
9. LaBean, T. *et al.* The construction, analysis, ligation and self-assembly of DNA triple crossover complexes. *J. Am. Chem. Soc.* **122,** 1848–1860 (2000).
10. Seeman, N. C. Nucleic acid nanostructures and topology. *Angew. Chem. Int. Edn Engl.* **37,** 3220–3238 (1998).
11. Faulhammer, D., Cukras, A. R., Lipton, R. J. & Landweber, L. F. Molecular computation: RNA solutions to chess problems. *Proc. Natl Acad. Sci. USA* **97,** 1385–1389 (2000).
12. Harada, K. & Orgel, L. E. Unexpected substrate specificity of T4 DNA ligase revealed by *in vitro* selection. *Nucleic Acids Res.* **21,** 2287–2291 (1993).
13. Winfree, E., Yang, X. & Seeman, N. C. in *DNA Based Computers: II Proceedings of a DIMACS Workshop, June 10–12, 1996, Princeton University* (eds Landweber, L. F. & Baum, E. B.) 217–254 (American Mathematical Society, Providence, RI, 1999).
14. Liu, Q. *et al.* DNA computing on surfaces. *Nature* **403,** 175–179 (2000).
15. Pirrung, M. C. *et al.* The arrayed primer extension method for DNA microchip analysis. Molecular computation of satisfaction problems. *J. Am. Chem. Soc.* **122,** 1873–1882 (2000).
16. Sakamoto, K. *et al.* Molecular computation by DNA hairpin formation. *Science* **288,** 1223–1226 (2000).
17. Gehani, A., LaBean, T. H. & Reif, J. H. in *DNA Based Computers: Proceedings of a DIMACS Workshop, June 1999, MIT* (ed. E. Winfree) (DIMACS Series in Discrete Mathematics and Theoretical Computer Science, American Mathematical Society, Providence, RI, in the press).
18. Reif, J. H. in *DNA Based Computers: III Proceedings of a DIMACS Workshop, June 23–25, 1997, University of Pennsylvania* (eds Rubin, H. & Wood D. H.) 217–254 (American Mathematical Society, Providence, RI, 1999).

Supplementary information is available on *Nature*'s World-Wide Web site (http://www.nature.com) or as paper copy from the London editorial office of *Nature*.

Acknowledgements

We thank E. Winfree and A. Carbone for valuable discussions. This work has been supported by grants from DARPA and the National Science Foundation to J.H.R. and N.C.S.; ONR, USAF, NSF and NIH grants to N.C.S.; and NSF and ARO grants to J.H.R.

Correspondence and requests for materials should be addressed to N.C.S. (e-mail: ned.seeman@nyu.edu).

Nano-sized transition-metal oxides as negative-electrode materials for lithium-ion batteries

P. Poizot, S. Laruelle, S. Grugeon, L. Dupont & J-M. Tarascon

Laboratoire de Réactivité et Chimie des Solides, Université de Picardie Jules Verne, CNRS UPRES A 6007, 33 rue Saint Leu, F-80039, Amiens, France

Rechargeable solid-state batteries have long been considered an attractive power source for a wide variety of applications, and in particular, lithium-ion batteries are emerging as the technology of choice for portable electronics. One of the main challenges in the design of these batteries is to ensure that the electrodes maintain their integrity over many discharge–recharge cycles. Although promising electrode systems have recently been proposed[1–7], their lifespans are limited by Li-alloying agglomeration[8] or the growth of passivation layers[9], which prevent the fully reversible insertion of Li ions into the negative electrodes. Here we report that electrodes made of nanoparticles of transition-metal oxides (MO, where M is Co, Ni, Cu or Fe) demonstrate electrochemical capacities of 700 mA h g^{-1}, with 100% capacity retention for up to 100 cycles and high recharging rates. The mechanism of Li reactivity differs from the classical Li insertion/deinsertion or Li-alloying processes, and involves the formation and decomposition of Li_2O, accompanying the reduction and oxidation of metal nanoparticles (in the range 1–5 nanometres) respectively. We expect that the use of transition-metal nanoparticles to enhance surface electrochemical reactivity will lead to further improvements in the performance of lithium-ion batteries.

intramolecular mechanism is also feasible (Fig. 5a). We obtained strong evidence for a dissociative mechanism by measuring the rate of dimelamine exchange between assemblies $\mathbf{1}_3\cdot(\mathrm{BuCYA})_6$ and $\mathbf{2}_3\cdot(\mathrm{BuCYA})_6$ by ^{1}H NMR spectroscopy. Upon mixing these assemblies in a 1:1 ratio in benzene-d_6 at 70 °C, well-separated signals for the new heteromeric assemblies $\mathbf{1}_2\mathbf{2}_1\cdot(\mathrm{BuCYA})_6$ and $\mathbf{1}_1\mathbf{2}_2\cdot(\mathrm{BuCYA})_6$ appear over time as a result of the exchange of calix[4]arene dimelamines **1** and **2**. The rate-determining step in the exchange process involves the dissociation of calix[4]arene dimelamines from an intact assembly, a process that requires the disruption of a total of 12 hydrogen bonds. If racemization occurred via a dissociative mechanism, the rates of dimelamine exchange and racemization should be of similar magnitude. We studied the concentration dependence of the rate of dimelamine exchange, both with and without (*S*)-BAR present, and found that this rate can be expressed by the same equation as the rate of racemization, with slightly different values of k_{cat} and k_{uncat} ($14.7 \times 10^{-3}\,\mathrm{l\,mol^{-1}\,s^{-1}}$ and $7.0 \times 10^{-5}\,\mathrm{s^{-1}}$, respectively, at 70 °C). These values relate well to those obtained from the racemization studies. (The slightly higher values for dimelamine exchange are due to the slightly higher temperature at which these ^{1}H NMR experiments were conducted, 70 versus 50 °C). From these results we conclude that racemization occurs predominantly via a dissociative mechanism, both uncatalysed and catalysed (Fig. 5b and c). The rate-limiting step involves the dissociation of calix[4]arene dimelamines from the intact assembly, followed by rapid racemization and formation of the opposite enantiomer. □

Received 17 March; accepted 4 September 2000.

1. Lehn, J.-M. *Supramolecular Chemistry, Concepts and Perspectives* (VCH, Weinheim, 1995).
2. Whitesides, G. M. *et al.* Noncovalent synthesis: using physical-organic chemistry to make aggregates. *Acc. Chem. Res.* **28,** 37–44 (1995).
3. Piguet, C., Bernardinelli, G. & Hopfgartner, G. Helicates as versatile supramolecular complexes. *Chem. Rev.* **97,** 2005–2062 (1997)
4. Yashima, E., Maeda, K. & Okamoto, Y. Memory of macromolecular helicity assisted by interaction with achiral small molecules. *Nature* **399,** 449–451 (1999).
5. Furusho, Y., Kimura, T., Mizuno, Y. & Aida, T. Chirality-memory molecule: a D_2-symmetric fully substituted porphyrin as a conceptually new chirality sensor. *J. Am. Chem. Soc.* **119,** 5267–5268 (1997).
6. Prins, L. J., Huskens, J., De Jong, F., Timmerman, P. & Reinhoudt, D. N. Complete asymmetric induction of supramolecular chirality in a hydrogen-bonded assembly. *Nature* **398,** 498–502 (1999).
7. Suárez, M., Branda, N., Lehn, J.-M., Decian, A. & Fischer, J. Supramolecular chirality: chiral hydrogen-bonded supermolecules from achiral molecular components. *Helv. Chim. Acta* **81,** 1–13 (1998).
8. Rivera, J. M., Martin, T. & Rebek, J. Jr Chiral spaces: dissymmetric capsules through self-assembly. *Science* **279,** 1021–1023 (1998).
9. Castellano, R. K., Nuckolls, C. & Rebek, J. Jr Transfer of chiral information through molecular assembly. *J. Am. Chem. Soc.* **121,** 11156–11163 (1999).
10. Qiao, S., Choi, I. S. & Whitesides, G. M. Observation of diastereomers of the hydrogen-bonded aggregate $\mathrm{Hub(M)_3}$.3CA using ^{1}H NMR spectroscopy when CA is an optically-active isocyanuric acid. *J. Org. Chem.* **62,** 2619–2621 (1997).
11. Prins, L. J., Jolliffe, K. A., Hulst, R., Timmerman, P. & Reinhoudt, D. N. Control of structural isomerism in noncovalent hydrogen bonded assemblies using peripheral chiral information. *J. Am. Chem. Soc.* **122,** 3617–3627 (2000).
12. Vreekamp, R. H., Van Duynhoven, J. P. M., Hubert, M., Verboom, W. & Reinhoudt, D. N. Molecular boxes based on calix[4]arene double rosettes. *Angew. Chem. Int. Edn Engl.* **35,** 1215–1218 (1996).
13. Timmerman, P. *et al.* Noncovalent assembly of functional groups on calix[4]arene molecular boxes. *Chem. Eur. J.* **3,** 1823–1832 (1997).
14. Jolliffe, K. A. *et al.* Characterization of supramolecular hydrogen-bonded assemblies by MALDI-TOF mass spectrometry after Ag^+-labelling. *Angew. Chem. Int. Edn Engl.* **37,** 1294–1297 (1998).
15. Mascal, M. *et al.* The ion-pair reinforced, hydrogen-bonding molecular ribbon. *J. Chem. Soc. Chem. Commun.* 805–806 (1995).
16. Shieh, H. S. & Voet, D. The x-ray structure of the molecular complex 8-bromo-9-ethyladenine-cyanuric acid monohydrate. *Acta Crystallogr. B* **32,** 2354–2360 (1976).
17. Yashima, E., Matsushima, T. & Okamoto, Y. Chirality assignment of amines and amino alcohols based on circular dichroism induced by helix formation of a stereoregular poly((4-carboxyphenyl)acetylene) through acid-base complexation. *J. Am. Chem. Soc.* **119,** 6345–6359 (1997).
18. Palmans, A. R. A., Vekemans, J. A. J. M., Havinga, E. E. & Meijer, E. W. Sergeants-and-soldiers principle in chiral columnar stacks of disc-shaped molecules with C_3 symmetry. *Angew. Chem. Int. Edn Engl.* **36,** 2648–2651 (1997).
19. Green, M. M. *et al.* A helical polymer with a cooperative response to chiral information. *Science* **268,** 1860–1866 (1995).

Supplementary Information is available on *Nature*'s World-Wide Web site (http://www.nature.com) or as paper copy from the London editorial office of *Nature*.

Acknowledgements

We thank C. Marjo and A. Bielejewska for their work on the model complexes **4·5** and **4·6**, and R. Fokkens and N.M.M. Nibbering for the MALDI-TOF MS measurements. This work was supported by the Council for Chemical Sciences of the Netherlands Organization for Scientific Research (CW-NWO).

Correspondence and requests for materials should be addressed to D.N.R. (e-mail: smct@ct.utwente.nl).

Acceleration of global warming due to carbon-cycle feedbacks in a coupled climate model

Peter M. Cox*, Richard A. Betts*, Chris D. Jones*, Steven A. Spall* & Ian J. Totterdell†

* *Hadley Centre, The Met Office, Bracknell, Berkshire RG12 2SY, UK*
† *Southampton Oceanography Centre, European Way, Southampton SO14 3ZH, UK*

The continued increase in the atmospheric concentration of carbon dioxide due to anthropogenic emissions is predicted to lead to significant changes in climate[1]. About half of the current emissions are being absorbed by the ocean and by land ecosystems[2], but this absorption is sensitive to climate[3,4] as well as to atmospheric carbon dioxide concentrations[5], creating a feedback loop. General circulation models have generally excluded the feedback between climate and the biosphere, using static vegetation distributions and CO_2 concentrations from simple carbon-cycle models that do not include climate change[6]. Here we present results from a fully coupled, three-dimensional carbon–climate model, indicating that carbon-cycle feedbacks could significantly accelerate climate change over the twenty-first century. We find that under a 'business as usual' scenario, the terrestrial biosphere acts as an overall carbon sink until about 2050, but turns into a source thereafter. By 2100, the ocean uptake rate of 5 Gt C yr^{-1} is balanced by the terrestrial carbon source, and atmospheric CO_2 concentrations are 250 p.p.m.v. higher in our fully coupled simulation than in uncoupled carbon models[2], resulting in a global-mean warming of 5.5 K, as compared to 4 K without the carbon-cycle feedback.

The general circulation model (GCM) that we used is based on the third Hadley Centre coupled ocean–atmosphere model, HadCM3[7], which we have coupled to an ocean carbon-cycle model (HadOCC) and a dynamic global vegetation model (TRIFFID). The atmospheric physics and dynamics of our GCM are identical to those used in HadCM3, but the additional computational expense of including an interactive carbon cycle made it necessary to reduce the ocean resolution to 2.5° × 3.75°, necessitating the use of flux adjustments in the ocean component to counteract climate drift. HadOCC accounts for the atmosphere–ocean exchange of CO_2, and the transfer of CO_2 to depth through both the solubility pump and the biological pump[8]. TRIFFID models the state of the biosphere in terms of the soil carbon, and the structure and coverage of five functional types of plant within each model gridbox (broadleaf tree, needleleaf tree, C_3 grass, C_4 grass and shrub). Further details on HadOCC and TRIFFID are given in Methods.

The coupled climate/carbon-cycle model was brought to equilibrium with a 'pre-industrial' atmospheric CO_2 concentration of 290 p.p.m.v., starting from an observed landcover data set[9]. The resulting state was stable, with negligible net land–atmosphere and

ocean–atmosphere carbon fluxes in the long-term mean, and no discernible drift in atmospheric CO_2 concentration. This simulation produces the locations of the main land biomes, and estimates of ocean carbon (38,100 Gt C), vegetation carbon (493 Gt C), soil carbon (1,180 Gt C) and terrestrial net primary productivity (60 Gt C yr^{-1}) that are within the range of other estimates[2,10–12]. Ocean primary productivity is also compatible with results derived from remote sensing[13,14], producing a global-mean total of 53 Gt C yr^{-1}, and realistic seasonal and latitudinal variations[15].

The simulated carbon cycle displays significant interannual variability, which is driven by the model-generated El Niño/Southern Oscillation (ENSO). A realistic response to internal climate variability is an important prerequisite for any carbon-cycle model to be used in climate change predictions. Fluctuations in annual-mean atmospheric CO_2 are correlated with the phase of ENSO, as indicated by the Nino3 index (Fig. 1). During El Niño conditions (positive Nino3), the model simulates an increase in atmospheric CO_2; this increase results from the terrestrial biosphere acting as a large source (especially in Amazonia[16]), which is only partially offset by a reduced outgassing from the tropical Pacific Ocean. The opposite is true during the La Niña phase. The overall sensitivity of the modelled carbon cycle to ENSO variability is consistent with the observational record[17], demonstrating that the coupled system responds realistically to climate anomalies.

Transient simulations were carried out for 1860–2100, using CO_2 emissions as given by the IS92a scenario[18]. Other greenhouse gases were also prescribed from IS92a, but the radiative effects of sulphate aerosols were omitted. Three separate runs were completed to isolate the effect of climate/carbon-cycle feedbacks; an experiment with prescribed IS92a CO_2 and fixed vegetation (that is, a 'standard' GCM climate change simulation), an experiment with interactive CO_2 and dynamic vegetation but no direct effects of CO_2 on climate (akin to 'offline' carbon-cycle projections that neglect climate change[6]), and a fully coupled climate/carbon-cycle simulation.

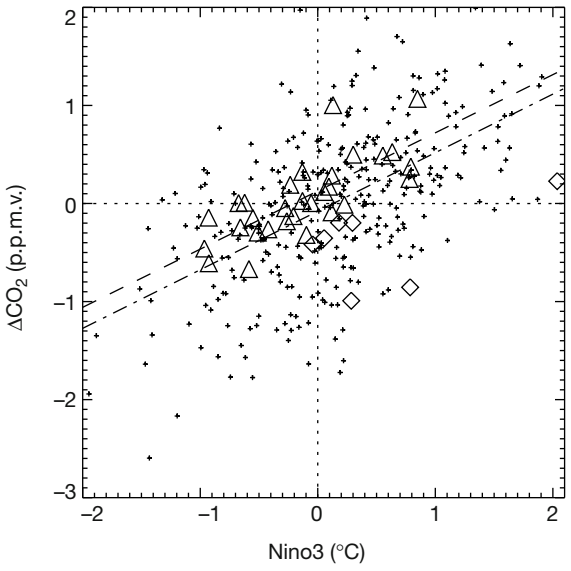

Figure 1 Modelled and observed interannual variability in the atmospheric CO_2 concentration. The figure shows the anomaly in the growth rate of atmospheric CO_2 versus the Nino3 index, taken from our pre-industrial control simulation (crosses) and the Mauna Loa observations (triangles). (The Nino3 index is the annual mean sea surface temperature anomaly in the tropical Pacific, 150° W–90° W, 5° S–5° N.) The gradients of the dashed and dot-dashed lines represent the sensitivity of the carbon cycle to ENSO, as given by the observations and the model, respectively. We have excluded observations that immediately follow major volcanic events (data points shown by diamonds), since during these years the carbon cycle may have been significantly perturbed by the induced tropospheric cooling.

Figure 2 shows results from the fully coupled run. From 1860 to 2000, the simulated stores of carbon in the ocean and on land increase by about 100 Gt C and 75 Gt C, respectively. However, the atmospheric CO_2 is 15–20 p.p.m.v. too high by the present day (corresponding to a timing error of about 10 years). Possible reasons for this include an overestimate of the prescribed net land-use emissions and the absence of other important climate forcing factors. The modelled global mean temperature increase from 1860 to 2000 is about 1.4 K (Fig. 3b), which is higher than observed[19], probably due to the absence of cooling from anthropogenic aerosols[20]. Offline tests suggest that such a relative warming can suppress the terrestrial carbon sink by enhancing soil and plant respiration[11]. Nevertheless, the rate of increase of CO_2 from 1950 to 2000 closely follows the recent observational record, which implies that the airborne fraction is being well simulated over this period. For the 20 years centred on 1985, the mean land and ocean uptake of carbon are 1.5 and 1.6 Gt yr^{-1}, respectively (compare best estimates for the 1980s of 1.8 ± 1.8 and 2.0 ± 0.8 Gt yr^{-1})[2]. The model therefore captures the most important characteristics of the present-day carbon cycle.

The simulated atmospheric CO_2 diverges much more rapidly from the standard IS92a concentration scenario in the future. First, vegetation carbon in South America begins to decline, as a drying and warming of Amazonia initiates loss of forest (Fig. 4a). This is driven purely by climate change, as can be seen by comparing the fully coupled run (red lines) to the run without global warming (blue lines). The effects of anthropogenic deforestation on land-cover are neglected in both cases. A second critical point is reached at about 2050, when the land biosphere as a whole switches from being a weak sink for CO_2 to being a strong source (Fig. 2). The reduction in terrestrial carbon from around 2050 onward is associated with a widespread climate-driven loss of soil carbon (Fig. 4b). An increase in the concentration of atmospheric CO_2 alone tends to increase the rate of photosynthesis and thus terrestrial carbon storage, provided that other resources are not limiting[4]. However, plant maintenance and soil respiration rates both increase with temperature. As a consequence, climate warming (the indirect effect of a CO_2 increase) tends to reduce terrestrial carbon storage[11], especially in the warmer regions where an increase in temperature is

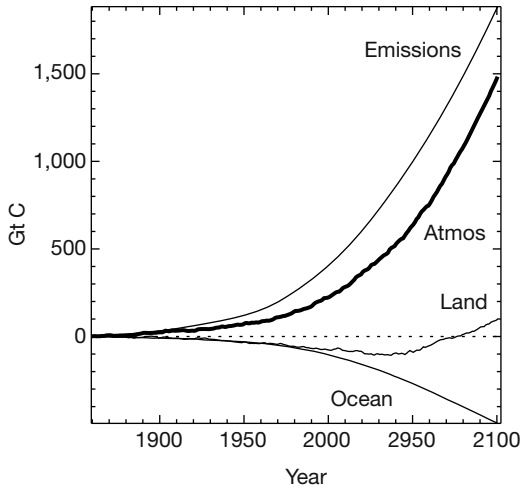

Figure 2 Budgets of carbon during the fully coupled simulation. The thick line shows the simulated change in atmospheric CO_2. The thinner lines show the integrated impact of the emissions, and of land and ocean fluxes, on the atmospheric CO_2 increase, with negative values implying net uptake of CO_2. We note that the terrestrial biosphere takes up CO_2 at a decreasing rate from about 2010 onwards, becoming a net source at around 2050. By 2100 this source from the land almost balances the oceanic sink, so that atmospheric carbon content is increasing at about the same rate as the integrated emissions (that is, the airborne fraction is ~1).

not beneficial for photosynthesis. At low CO_2 concentrations the direct effect of CO_2 dominates, and both vegetation and soil carbon increase with atmospheric CO_2. But as CO_2 increases further, terrestrial carbon begins to decrease, because the direct effect of CO_2 on photosynthesis saturates but the specific soil respiration rate continues to increase with temperature. The transition between these two regimes occurs abruptly at around 2050 in this experiment (Fig. 4b). The carbon stored on land decreases by about 170 Gt C from 2000 to 2100, accelerating the rate of atmospheric CO_2 increase over this period.

The ocean takes up about 400 Gt C over the same period, but at a rate which is asymptotically approaching 5 Gt C yr^{-1} by 2100. This reduced efficiency of oceanic uptake is partly a consequence of the nonlinear dependence of the partial pressure of dissolved CO_2 on the total ocean carbon concentration, but may also have contributions from climate change[3]. Although the thermohaline circulation of the ocean weakens[21] by about 25% from 2000 to 2100, this is much less of a reduction than seen in some previous simulations[22], and the corresponding effect on ocean carbon uptake is less significant. In our experiment, increased thermal stratification due to warming of the sea surface suppresses upwelling, which reduces nutrient availability and lowers primary production by about 5%. However, ocean-only tests suggest a small effect of climate change on oceanic carbon uptake, as this reduction in the biological pump is compensated by reduced upwelling of deep waters which have high concentrations of total carbon.

By 2100 the modelled CO_2 concentration is about 980 p.p.m.v. in the coupled experiment, which is more than 250 p.p.m.v. higher than the standard IS92a scenario or that simulated in the 'offline' experiment (Fig. 3a). As a result, the global-mean land temperatures increase from 1860 to 2100 by about 8 K, rather than the 5.5 K of the standard scenario (Fig. 3b).

These numerical experiments demonstrate the potential importance of climate/carbon-cycle feedbacks, but the magnitude of these in the real Earth system is still highly uncertain. Terrestrial carbon models differ in their responses to climate change[11,12], owing to gaps in basic understanding of processes. For example, the potential conversion of the global terrestrial carbon sink to a source is critically dependent upon the long-term sensitivity of soil respiration to global warming, which is still a subject of debate[23]. The experiments presented here exclude the potentially large direct human influences on terrestrial carbon uptake through changes in landcover and land management. Local effects, such as the possible climate-driven loss of the Amazon rainforest, rest upon uncertain aspects of regional climate change, and may be 'short-circuited' by direct human deforestation. A full assessment of the uncertainties must await further coupled experiments utilizing alternative representations of processes and including a more complete set of natural

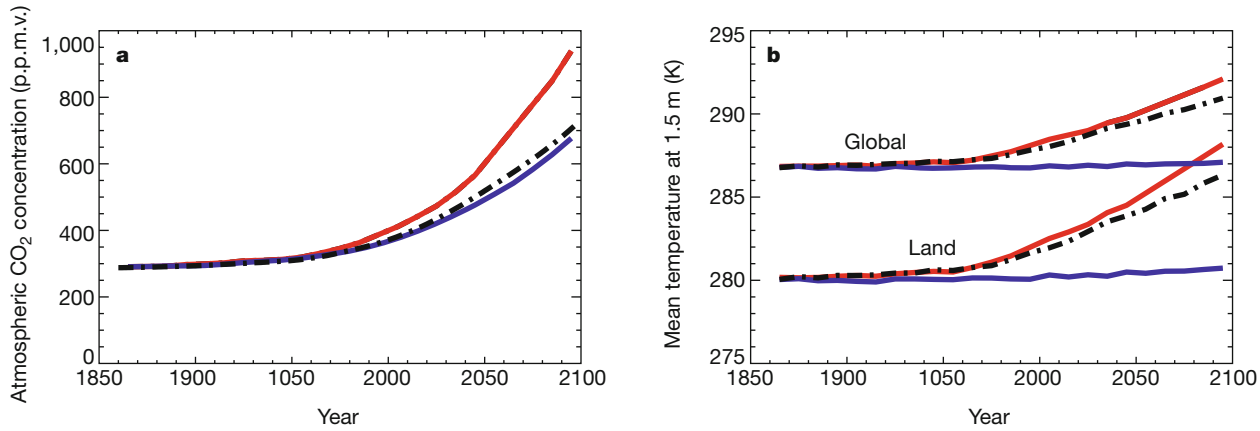

Figure 3 Effect of climate/carbon-cycle feedbacks on CO_2 increase and global warming. **a**, Global-mean CO_2 concentration, and **b**, global-mean and land-mean temperature, versus year. Three simulations are shown; the fully coupled simulation with interactive CO_2 and dynamic vegetation (red lines), a standard GCM climate change simulation with prescribed (IS92a) CO_2 concentration and fixed vegetation (dot-dashed lines), and the simulation which neglects direct CO_2-induced climate change (blue lines). The slight warming in the latter is due to CO_2-induced changes in stomatal conductance and vegetation distribution.

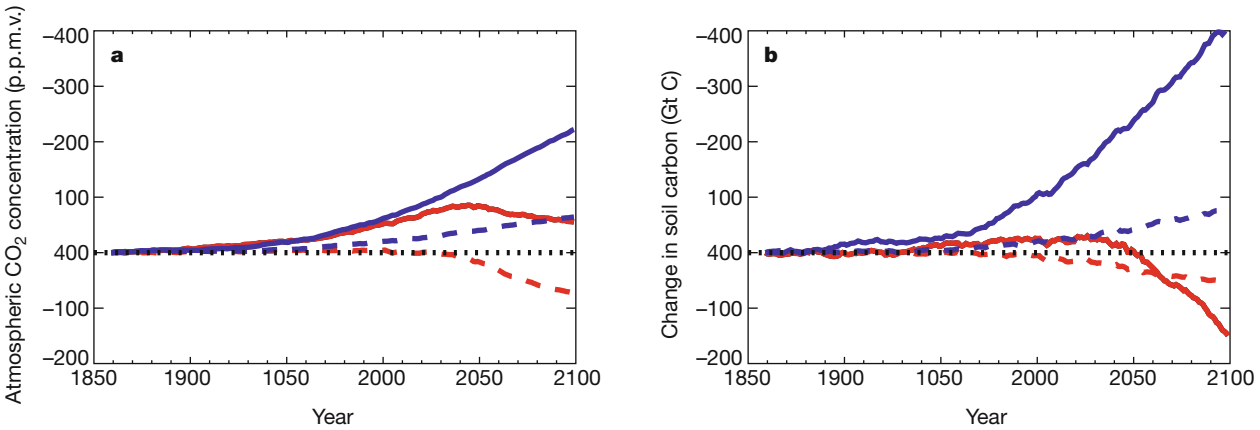

Figure 4 Effect of global warming on changes in land carbon storage. The red lines represent the fully coupled climate/carbon-cycle simulation, and the blue lines are from the 'offline' simulation which neglects direct CO_2-induced climate change. The figure shows simulated changes in vegetation carbon (**a**) and soil carbon (**b**) for the global land area (continuous lines) and South America alone (dashed lines).

and anthropogenic forcing factors (for example, land-use change, forest fires, sulphate aerosol concentrations and nitrogen deposition). However, our results indicate that it will be essential to accurately represent previously neglected carbon-cycle feedbacks if we are to successfully predict climate change over the next 100 years. □

Methods

Ocean carbon-cycle model

The inorganic component of HadOCC has been extensively tested as part of the Ocean Carbon Cycle Intercomparison Project; it was found to reproduce tracer distributions to an accuracy consistent with other ocean GCMs[24]. The biological component treats four additional ocean fields: nutrient, phytoplankton, zooplankton and detritus[8]. The phytoplankton population changes as a result of the balance between growth, which is controlled by light level and the local concentration of nutrient, and mortality, which is mostly as a result of grazing by zooplankton. Detritus, which is formed by zooplankton excretion and by phyto- and zooplankton mortality, sinks at a fixed rate and slowly remineralizes to reform nutrient and dissolved inorganic carbon. Thus both nutrient and carbon are absorbed by phytoplankton near the ocean surface, pass up the food chain to zooplankton, and are eventually remineralized from detritus in the deeper ocean. The model also includes the formation of calcium carbonate and its dissolution at depth (below the lysocline).

Terrestrial carbon-cycle model

TRIFFID (top-down representation of interactive foliage and flora including dynamics) has been used offline in a comparison of dynamic global vegetation models[11]. Carbon fluxes for each vegetation type are calculated every 30 minutes as a function of climate and atmospheric CO_2 concentration, from a coupled photosynthesis/stomatal-conductance scheme[25,26], which utilizes existing models of leaf-level photosynthesis in C_3 and C_4 plants[27,28]. The accumulated fluxes are used to update the vegetation and soil carbon every 10 days. The natural landcover evolves dynamically based on competition between the vegetation types, which is modelled using a Lotka–Volterra approach and a tree–shrub–grass dominance hierarchy. We also prescribe some agricultural regions, in which grasslands are assumed to be dominant. Carbon lost from the vegetation as a result of local litterfall or large-scale disturbance is transferred into a soil carbon pool, where it is broken down by microorganisms that return CO_2 to the atmosphere. The soil respiration rate is assumed to double for every 10 K of warming[29], and is also dependent on the soil moisture content[30]. Changes in the biophysical properties of the land surface[5], as well as changes in terrestrial carbon, feed back onto the atmosphere.

Received 6 January; accepted 26 September 2000.

1. Houghton, J. T. *et al.* (eds) *Climate Change 1995: The Science of Climate Change* (Cambridge Univ. Press, Cambridge, 1996).
2. Schimel, D. *et al.* in *Climate Change 1995: The Science of Climate Change* Ch. 2 (eds Houghton, J. T. *et al.*) 65–131 (Cambridge Univ. Press, Cambridge, 1995).
3. Sarmiento, J., Hughes, T., Stouffer, R. & Manabe, S. Simulated response of the ocean carbon cycle to anthropogenic climate warming. *Nature* **393,** 245–249 (1998).
4. Cao, M. & Woodward, F. I. Dynamic responses of terrestrial ecosystem carbon cycling to global climate change. *Nature* **393,** 249–252 (1998).
5. Betts, R. A., Cox, P. M., Lee, S. E. & Woodward, F. I. Contrasting physiological and structural vegetation feedbacks in climate change simulations. *Nature* **387,** 796–799 (1997).
6. Enting, I., Wigley, T. & Heimann, M. *Future Emissions and Concentrations of Carbon Dioxide; Key Ocean/Atmosphere/Land Analyses* (Technical Paper 31, Division of Atmospheric Research, CSIRO, Melbourne, 1994).
7. Gordon, C. *et al.* The simulation of SST, sea ice extents and ocean heat transports in a version of the Hadley Centre coupled model without flux adjustments. *Clim. Dyn.* **16,** 147–168 (2000).
8. Palmer, J. R. & Totterdell, I. J. Production and export in a global ocean ecosystem model. *Deep-Sea Res.* (in the press).
9. Wilson, M. F. & Henderson-Sellers, A. A global archive of land cover and soils data for use in general circulation climate models. *J. Clim.* **5,** 119–143 (1985).
10. Zinke, P. J., Stangenberger, A. G., Post, W. M., Emanuel, W. R. & Olson, J. S. *Worldwide Organic Soil Carbon and Nitrogen Data* (NDP-018, Carbon Dioxide Information Center, Oak Ridge National Laboratory, Oak Ridge, Tennessee, 1986).
11. Cramer, W. *et al.* Global response of terrestrial ecosystem structure and function to CO_2 and climate change: results from six dynamic global vegetation models. *Glob. Change Biol.* (in the press).
12. VEMAP Members. Vegetation/ecosystem modelling and analysis project: comparing biogeography and biogeochemistry models in a continental-scale study of terrestrial responses to climate change and CO_2 doubling. *Glob. Biogeochem. Cycles* **9,** 407–437 (1995).
13. Longhurst, A., Sathyendranath, S., Platt, T. & Caverhill, C. An estimate of global primary production in the ocean from satellite radiometer data. *J. Plank. Res.* **17,** 1245–1271 (1995).
14. Field, C., Behrenfeld, M., Randerson, J. & Falkowski, P. Primary production of the biosphere: integrating terrestrial and oceanic components. *Science* **281,** 237–240 (1998).
15. Antoine, D., Andre, J.-M. & Morel, A. Oceanic primary production 2. Estimation at global scale from satellite (Coastal Zone Color Scanner) chlorophyll. *Glob. Biogeochem. Cycles* **10,** 57–69 (1996).
16. Tian, H. *et al.* Effects of interannual climate variability on carbon storage in Amazonian ecosystems. *Nature* **396,** 664–667 (1998).
17. Keeling, C. D., Whorf, T., Whalen, M. & der Plicht, J. V. Interannual extremes in the rate of rise of atmospheric carbon dioxide since 1980. *Nature* **375,** 666–670 (1995).
18. Houghton, J. T., Callander, B. A. & Varney, S. K. (eds) *Climate Change 1992: The Supplementary Report to the IPCC Scientific Assessment* (Cambridge Univ. Press, Cambridge, 1992).
19. Nicholls, N. *et al.* in *Climate Change 1995: The Science of Climate Change* Ch. 3 (eds Houghton, J. T. *et al.*) (Cambridge Univ. Press, Cambridge, 1996).
20. Mitchell, J. F. B., Johns, T. C., Gregory, J. M. & Tett, S. F. B. Climate response to increasing levels of greenhouse gases and sulphate aerosols. *Nature* **376,** 501–504 (1995).
21. Wood, R. A., Keen, A. B., Mitchell, J. F. B. & Gregory, J. M. Changing spatial structure of the thermohaline circulation in response to atmospheric CO_2 forcing in a climate model. *Nature* **399,** 572–575 (1999).
22. Sarmiento, J. & Quere, C. L. Oceanic carbon dioxide uptake in a model of century-scale global warming. *Nature* **274,** 1346–1350 (1996).
23. Giardina, C. & Ryan, M. Evidence that decomposition rates of organic carbon in mineral soil do not vary with temperature. *Nature* **404,** 858–861 (2000).
24. Orr, J. C. in *Ocean Storage of Carbon Dioxide, Workshop 3: International Links and Concerns* (ed. Ormerod, W.) 33–52 (IEA R&D Programme, CRE Group Ltd, Cheltenham, UK, 1996).
25. Cox, P. M., Huntingford, C. & Harding, R. J. A canopy conductance and photosynthesis model for use in a GCM land surface scheme. *J. Hydrol.* **212–213,** 79–94 (1998).
26. Cox, P. M. *et al.* The impact of new land surface physics on the GCM simulation of climate and climate sensitivity. *Clim. Dyn.* **15,** 183–203 (1999).
27. Collatz, G. J., Ball, J. T., Grivet, C. & Berry, J. A. Physiological and environmental regulation of stomatal conductance, photosynthesis and transpiration: a model that includes a laminar boundary layer. *Agric. Forest Meteorol.* **54,** 107–136 (1991).
28. Collatz, G. J., Ribas-Carbo, M. & Berry, J. A. A coupled photosynthesis-stomatal conductance model for leaves of C4 plants. *Aust. J. Plant Physiol.* **19,** 519–538 (1992).
29. Raich, J. & Schlesinger, W. The global carbon dioxide flux in soil respiration and its relationship to vegetation and climate. *Tellus B* **44,** 81–99 (1992).
30. McGuire, A. *et al.* Interactions between carbon and nitrogen dynamics in estimating net primary productivity for potential vegetation in North America. *Glob. Biogeochem. Cycles* **6,** 101–124 (1992).

Acknowledgements

We thank J. Mitchell and G. Jenkins for comments on earlier versions of the manuscript. This work was supported by the UK Department of the Environment, Transport and the Regions.

Correspondence and requests for materials should be addressed to P.M.C. (e-mail: pmcox@meto.gov.uk).

Offset of the potential carbon sink from boreal forestation by decreases in surface albedo

Richard A. Betts

Hadley Centre for Climate Prediction and Research, The Met Office, Bracknell, Berkshire RG12 2SY, UK

Carbon uptake by forestation is one method proposed[1] to reduce net carbon dioxide emissions to the atmosphere and so limit the radiative forcing of climate change[2]. But the overall impact of forestation on climate will also depend on other effects associated with the creation of new forests. In particular, the albedo of a forested landscape is generally lower than that of cultivated land, especially when snow is lying[3–9], and decreasing albedo exerts a positive radiative forcing on climate. Here I simulate the radiative forcings associated with changes in surface albedo as a result of forestation in temperate and boreal forest areas, and translate these forcings into equivalent changes in local carbon stock for comparison with estimated carbon sequestration potentials[10–12]. I suggest that in many boreal forest areas, the positive forcing induced by decreases in albedo can offset the negative forcing that is expected from carbon sequestration. Some high-latitude forestation activities may therefore increase climate change, rather than mitigating it as intended.

Perturbations to the balance between radiation absorbed and emitted by the Earth ('radiative forcing') can result from changes in atmospheric chemistry and planetary albedo. A positive 'greenhouse' forcing results from increased atmospheric CO_2 absorbing and re-emitting more of the infrared radiation emitted by the surface[13]; forestation may help to mitigate this by slowing the rise

1958–88 (see above). Matching data from 8 trees sampled on the east end of Isle Royale, where balsam fir are not heavily or repeatedly browsed by moose[10], provided a natural control for the test of our hypothesis relating climate and wolf behaviour to the dynamics of moose and fir growth. On the east end, fir growth did not correlate with the NAO index at lags of 0 ($r = 0.074$, $P = 0.69$) or 1 year ($r = 0.069$, $P = 0.71$) or with moose density at a lag of 1 year ($r = 0.054$, $P = 0.78$).

The North Atlantic Oscillation

The NAO is a meridional alternation in atmospheric mass balance between pressure centres over the Azores and Iceland. The winter NAO index is calculated on the basis of the normalized sea-level pressure difference between these two centres from December to March[17]. A negative difference indicates weak westerly winds across the Atlantic Ocean and unusually warm winters over north eastern North America; opposing conditions prevail during positive years[17]. We used data from the Climate Indices website of the National Center for Atmospheric Research, Boulder, USA (http://www.cgd.ucar.edu/cas/climind/). Although annual snow depth measures during the study period are not available for Isle Royale, the NAO index correlates negatively with snow depth in nearby Superior National Forest, USA[9]. In all regressions, degrees of freedom for tests of significance of independent variables were adjusted for autocorrelation[9].

Received 24 March; accepted 11 August 1999.

1. Estes, J. A. & Palmisano, J. F. Sea otters: their role in structuring nearshore communities. *Science* **185,** 1058–1060 (1974).
2. Spiller, D. A. & Schoener, T. W. A terrestrial field experiment showing the impact of eliminating top predators on foliage damage. *Nature* **347,** 469–472 (1990).
3. McPeek, M. A. The consequences of changing the top predator in a food web: a comparative experimental approach. *Ecol. Monogr.* **68,** 1–23 (1998).
4. Sanford, E. Regulation of keystone predation by small changes in ocean temperature. *Science* **283,** 2095–2097 (1999).
5. Paine, R. T. Food web complexity and species diversity. *Am. Nat.* **100,** 65–75 (1966).
6. Paine, R. T. Intertidal community structure: Experimental studies on the relationship between a dominant competitor and its principal predator. *Oecologia* **15,** 93–120 (1974).
7. Estes, J. A. & Duggins, D. O. Sea otters and kelp forests in Alaska: generality and variation in a community ecological paradigm. *Ecol. Monogr.* **65,** 75–100 (1995).
8. Estes, J. A., Tinker, M. T., Williams, T. M. & Doak, D. F. Killer whale predation on sea otters linking oceanic and nearshore ecosystems. *Science* **282,** 473–476 (1998).
9. Post, E. & Stenseth, N. C. Large-scale climatic variability and population dynamics of moose and white-tailed deer. *J. Anim. Ecol.* **67,** 537–543 (1998).
10. McLaren, B. E. & Peterson, R. O. Wolves, moose, and tree rings on Isle Royale. *Science* **266,** 1555–1558 (1994).
11. Peterson, R. O. *Wolf Ecology and Prey Relationships on Isle Royale* (National Park Services Scientific Ser. No. 11, Washington DC, 1977).
12. Peterson, R. O., Page, R. E. & Dodge, K. M. Wolves, moose, and the allometry of population cycles. *Science* **224,** 1350–1352 (1984).
13. McLaren, B. E. & Janke, R. A. Seedbed and canopy cover effects on balsam fir seedling establishment in Isle Royale National Park. *Can. J. For. Res.* **26,** 782–793 (1996).
14. Brandner, T. A., Peterson, R. O. & Risenhoover, K. L. Balsam fir on Isle Royale: effects of moose herbivory and population density. *Ecology* **71,** 155–164 (1990).
15. McInnes, P. F., Naiman, R. J., Pastor, J. & Cohen, Y. Effects of moose browsing on vegetation and litter of the boreal forest, Isle Royale, Michigan, USA. *Ecology* **73,** 2059–2075 (1992).
16. Pastor, J., Dewey, B., Naiman, R. J., McInnes, P. F. & Cohen, Y. Moose browsing and soil fertility in the boreal forests of the Isle Royale National Park. *Ecology* **74,** 467–480 (1993).
17. Hurrell, J. W. Decadal trends in the North Atlantic Oscillation: regional temperatures and precipitation. *Science* **269,** 676–679 (1995).
18. Mech, L. D., McRoberts, R. E., Peterson, R. O. & Page, R. E. Relationship of deer and moose populations to previous winters' snow. *J. Anim. Ecol.* **56,** 615–627 (1987).
19. Post, E. & Stenseth, N. C. Climatic variability, plant phenology, and northern ungulates. *Ecology* **80,** 1322–1339.
20. Peterson, R. O., Thomas, J. N., Thurber, J. M., Vucetich, J. A. & Waite, T. A. Population limitation and the wolves of Isle Royale. *J. Mamm.* **79,** 828–841 (1998).
21. Thurber, J. M. & Peterson, R. O. Effects of population density and pack size on the foraging ecology of gray wolves. *J. Mamm.* **74,** 870–889 (1993).
22. Schmidt, P. A. & Mech, L. D. Wolf pack size and food acquisition. *Am. Nat.* **150,** 513–517 (1997).
23. Peterson, R. O. & Page, R. E. The rise and fall of Isle Royale wolves, 1975–1986. *J. Mamm.* **69,** 89–99 (1988).
24. Peterson, R. O. & Allen, D. L. Snow conditions as a parameter in moose-wolf relationships. *Le Naturaliste Canadien* **101,** 481–492 (1974).
25. Kelsall, J. P. Structural adaptations of moose and deer for snow. *J. Mamm.* **50,** 302–310 (1969).
26. Molvar, E. M. & Bowyer, R. T. Moose herbivory, browse quality, and nutrient cycling in an Alaskan treeline community. *Oecologia* **94,** 472–479 (1993).
27. Mech, L. D. *The Wolf* (Univ. Minnesota Press, 1970).
28. Ben-David, M., Bowyer, R. T., Duffy, L. K., Roby, D. D. & Schell, D. M. Social behavior and ecosystem processes: river otter latrines and nutrient dynamics of terrestrial vegetation. *Ecology* **79,** 2567–2571 (1998).
29. Beckerman, A. P., Uriarte, M. & Schmitz, O. J. Experimental evidence for a behavior-mediated trophic cascade in a terrestrial food chain. *Proc. Natl Acad. Sci. USA* **94,** 10735–10738 (1997).
30. Schmitz, O. J., Beckerman, A. P. & O'Brien, K. M. Behaviorally mediated trophic cascades: effects of predation risk on food web interactions. *Ecology* **78,** 1388–1399 (1997).

Acknowledgements

We thank the U.S. National Science Foundation for grants to E.P. and R.O.P., the US National Park Service and Earthwatch for grants to R.O.P. and the Norwegian Science Council (NFR) for a grant to N.C.S. We thank G.-P. Saetre for discussions.

Correspondence and requests for materials should be addressed to E.P. (e-mail: eric.post@bio.uio.no).

Allometric scaling of production and life-history variation in vascular plants

Brian J. Enquist*†, Geoffrey B. West†‡, Eric L. Charnov§ & James H. Brown§†

* *National Center for Ecological Analysis and Synthesis, 735 State Street, Suite 300, Santa Barbara, California 93101-5504, USA*
§ *Department of Biology, University of New Mexico, Albuquerque, New Mexico 87131, USA*
† *The Santa Fe Institute, 1399 Hyde Park Road, Santa Fe, New Mexico 87501, USA*
‡ *Theoretical Division, T-8, MS B285, Los Alamos National Laboratory, Los Alamos, New Mexico 87545, USA*

A prominent feature of comparative life histories is the well documented negative correlation between growth rate and life span[1,2]. Patterns of resource allocation during growth and reproduction reflect life-history differences between species[1,2]. This is particularly striking in tropical forests, where tree species can differ greatly in their rates of growth and ages of maturity but still attain similar canopy sizes[3,4]. Here we provide a theoretical framework for relating life-history variables to rates of production, dM/dt, where M is above-ground mass and t is time. As metabolic rate limits production as an individual grows, $dM/dt \propto M^{3/4}$. Incorporating interspecific variation in resource allocation to wood density, we derive a universal growth law that quantitatively fits data for a large sample of tropical tree species with diverse life histories. Combined with evolutionary life-history theory[1], the growth law also predicts several qualitative features of tree demography and reproduction. This framework also provides a general quantitative answer to why relative growth rate $(1/M)(dM/df)$ decreases with increasing plant size ($\propto M^{-1/4}$) and how it varies with differing allocation strategies[5–8].

Coexistence in diverse ecological communities has been thought to be due, in part, to life-history trade-offs involving allocation of resources[6,9–13]. There is, however, no generally accepted mechanistic framework for understanding how patterns of allocation influence variation in life histories. Here we show that a general allometric growth model for trees can provide an explanation for much life-history variation. Metabolism produces the energy and materials that are used for all biological processes. A central issue of life history is how over ontogeny the products of metabolism are allocated among maintenance, growth and reproduction. Previous work has shown how the 3/4-power scaling of metabolic rate with body mass in both animals and plants results from physical and biological constraints on the distribution of resources through fractal-like vascular networks[14–16].

In Box 1, we derive a production/growth law in terms of above-ground plant mass, M, or basal stem diameter, D. Our data set (Table 1, Fig. 1) consists of a 20-year change in D ($D(20)$ compared with $D(0)$) for 45 species of trees in a tropical dry forest. In total, there were 2,283 individuals, all of reproductive age. Equation (6) predicts that $D^{2/3}(20) = A_i + D^{2/3}(0)$, so that a plot of $D^{2/3}(20)$ versus $D^{2/3}(0)$ for each species should yield a straight line with a universal slope of unity and an intercept, A_i, inversely proportional to wood density, ρ, so that A_i is proportional to ρ^{-1}. We tested this prediction by analysing the data for 45 species (Fig. 2a, Table 1). The average slope of all species, 1.04, is essentially not different from the predicted value of 1.0 (95% confidence intervals (CI): 1.01 to 1.08). Forty of the forty-five species had slopes statistically indistinguishable from the predicted value of 1 (Table 1). There was no systematic trend to deviate above or below 1; furthermore, we expect 5% (≈2.5 species) to differ by chance alone at the 0.05 level.

We conclude that production within species scales as $M^{3/4}$. There is, however, considerable interspecific variation in the intercepts. From Box 1, the intercepts should be inversely proportional to wood density, ρ, and this is confirmed by regression analysis ($r = -0.468$, exponent $= -0.934$, 95% CI: -1.631 to -0.237, intercept $= 0.6196$, $n = 29$). Weighting each species by multiplying $D^{2/3}$ by ρ collapses the production relationships for each species onto a line with a universal slope of unity and a common intercept (see Fig. 2b and equation (6)). Essentially, there is a trade-off in growth rate (change in stem diameter) with allocation to tissue density: species that allocate less biomass to their stems (light woods) increase in basal diameter faster than species that allocate more to stems (dense woods).

The trees depicted in Fig. 2a are reproducing, so some proportion of production, λ, must be allocated to reproduction rather than growth. The derivation in Box 1 (resulting in equation (7)) and measured empirical reproductive allometries both suggest that λ is independent of size within a species. To obtain the convergence of allometries implied in Fig. 2b requires the stronger constraint that λ be the same across species. Studies reporting relationships between production of reproduction mass and stem diameter indicate that whereas measured exponents usually approximate to the predicted value of 2, there are differences in normalization constants, and hence in λ, among species[17–20]. Such variation will not change the predicted slope of unity when data are plotted as in Fig. 2a. If this variation in λ is independent of ρ, however, it will show up as residual variation in plots such as Fig. 2b.

Production data for seven species of temperate trees provide additional evidence that dM/dt is proportional to $M^{3/4}$. Instead of measuring change in diameter, Whittaker and Woodwell[21] recorded total annual mass production of leaves and twigs, and bark and stem wood as a function of trunk diameter. Relating trunk diameter to annual production for twig and leaf mass, and wood and bark mass, shows that both scale with exponents essentially indistinguishable from the predicted $M^{3/4}$. So mass production in both tropical and temperature trees scales as $M^{3/4}$.

Relative growth rate $(1/M)(dM/dt)$ decreases with increases in individual size and varies across species[5–8]. Although this decrease has been qualitatively attributed to several mechanisms[6], a quantitative rule emerges as a direct consequence of equations (2) and (3): $(1/M)(dM/dt) \propto M^{-1/4}$. This rule is predicted to hold even across species growing in the same environment for comparisons when

Box 1

The growth law

As trees continue to increase in size throughout life, and this growth must be fuelled by metabolism, it is reasonable to assume that the growth rate (the rate at which its mass, M, increases over time), is directly proportional to metabolic rate, B, (the rate of gross photosynthesis). Thus, at any time t,

$$\frac{dM}{dt} = C_G B \tag{2}$$

where C_G is a proportionality constant that can be time dependent. It has been shown that B is proportional to $V^{3/4}$, and stem diameter, D, is proportional to $V^{3/8}$, where V is the total volume of the plant[14]. If $\rho = (M/V)$ is the tissue- or species-specific wood density, then, at any time t, these can be expressed as

$$B = C_B\left(\frac{M}{\rho}\right)^{3/4} \qquad D = C_D\left(\frac{M}{\rho}\right)^{3/8} \tag{3}$$

where C_B and C_D are corresponding proportionality constants. Implicit in these results is the assumption that the ratio E/ρ, where E is the Young's modulus of elasticity, is constant for all plants[18]. Here, we relax the restriction implicit in ref. 14 that ρ is constant and allow it to differ among plant species and to vary with time. Equations (2) and (3) can be combined to give

$$\frac{dD}{dt} = \left(\frac{3C}{2\rho}\right)D^{1/3} \tag{4}$$

where $C \equiv 1/4 C_G C_B C_D^{2/3}$. This can be integrated to give

$$D(t)^{2/3} - D(t_0)^{2/3} = \int_{t_0}^{t} \frac{C(t)}{\rho(t)}dt \tag{5}$$

where the time dependence of all variables has been made explicit and the integration has been carried out from some initial time, t_0, up to some arbitrary time, t. Thus, regardless of any possible time dependence of either the proportionality constants or the density, a plot of $D^{2/3}(t)$ versus $D^{2/3}(t_0)$ for fixed times t and t_0 for any species should yield a straight line with a universal slope of unity but with an intercept that depends on the time interval and the species. If, however, ρ of a given plant is taken to be independent of time, but allowed to vary across species, this can be re-expressed as

$$\rho[D(t)^{2/3} - D(t_0)^{2/3}] = \int_{t_0}^{t} C(t)dt \tag{6}$$

The intercept of the production relationship should therefore be inversely proportional to ρ. If C_G, C_B, and C_D are independent of time then the intercept, namely the righthand side of equation (6), is given by $C(t - t_0)$. Furthermore, if C does not vary among species as implicitly assumed in ref. 14, and the time interval is the same for all species, then weighting $D^{2/3}(t)$ and $D^{2/3}(t_0)$ by ρ should collapse all species onto a universal line of unit slope. The intercept should no longer depend upon the species but only upon the time interval and C (however, see below for the reproductive period).

This framework allows us to recast the mass-production law as a function of basal stem diameter, D,

$$\frac{dM}{dt} = \left(\frac{C_G C_B}{C_D^2}\right)D^2 \tag{7}$$

This gives the new prediction that across species, dM/dt, for trees of the same diameter is explicitly independent of wood density ρ

The derivation so far has assumed that the plant is not reproducing, so that all production is given to growth. Growth must, however, slow with the onset of reproduction[1], as some fraction of production, $(\lambda)dM/dt$, is then devoted to reproduction rather than to individual growth, $(1 - \lambda)dM/dt$. The scaling rule for reproductive allocation and growth after the onset of reproduction depends upon the behaviour of λ. Life-history theory[1,2] predicts the age (size) course of this reproductive allocation. The simplest model is to take λ as a constant both within and across species. A constant λ within species is supported by several studies[17–20] that have measured allometries for the biomass of reproductive organs, M_R, versus stem diameter, D, in both angiosperms and gymnosperms. M_R reflects the rate of allocation to reproduction. Since published studies show that M_R is generally proportional to D^2, it follows from equation (7) that M_R is proportional to dM/dt indicating that λ is indeed approximately a constant within species and independent of size. This is an important result, as animals have λ increasing from 0 to 1 over the reproductive period[1,2]. The fact that trees appear to have nearly constant values of λ probably reflects the constraints of resource harvesting and biomechanics on plant growth and development. Note that if λ is approximately constant, all of the previous growth results are true for all time periods $(t - t_0)$ after the onset of reproduction, with C_G redefined to be $(1 - \lambda)C_G$.

wood density is held constant.

The simplest life-history theory assumes determinate growth: at the onset of reproduction all production ($\lambda = 1$) is given to reproduction and growth ceases[1]. If we approximate plant growth in this way and assume a pre-reproductive production rate $dM/dt = C_G B = C_G C_B (M/\rho)^{3/4}$ as in equations (2) and (3), and if mortality rate is independent of plant size (over a range which includes possible sizes at maturation), well known arguments[1] for

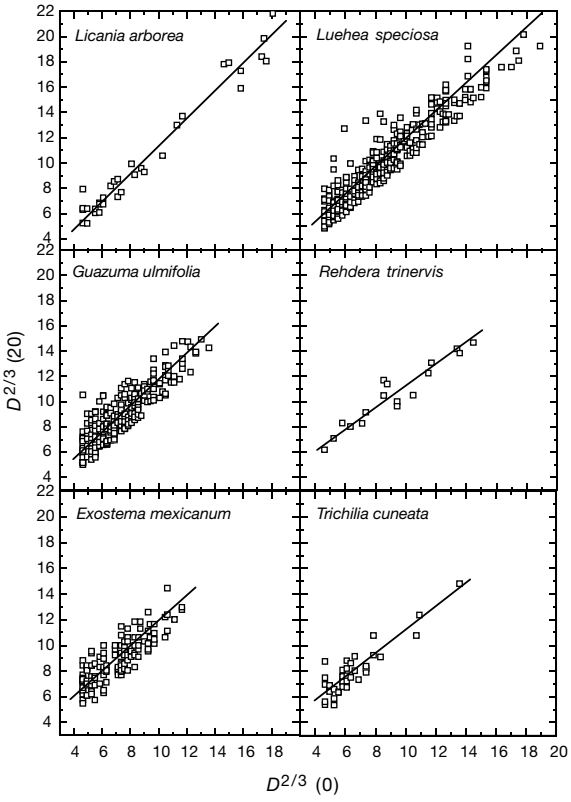

Figure 1 Representative variation of $D^{2/3}(0)$ versus $D^{2/3}(20)$ for six species of tropical trees. When sample sizes are large, the apparent variation is exaggerated because of the overlap of many points. Values for slopes and r^2 for these species are given in Table 1.

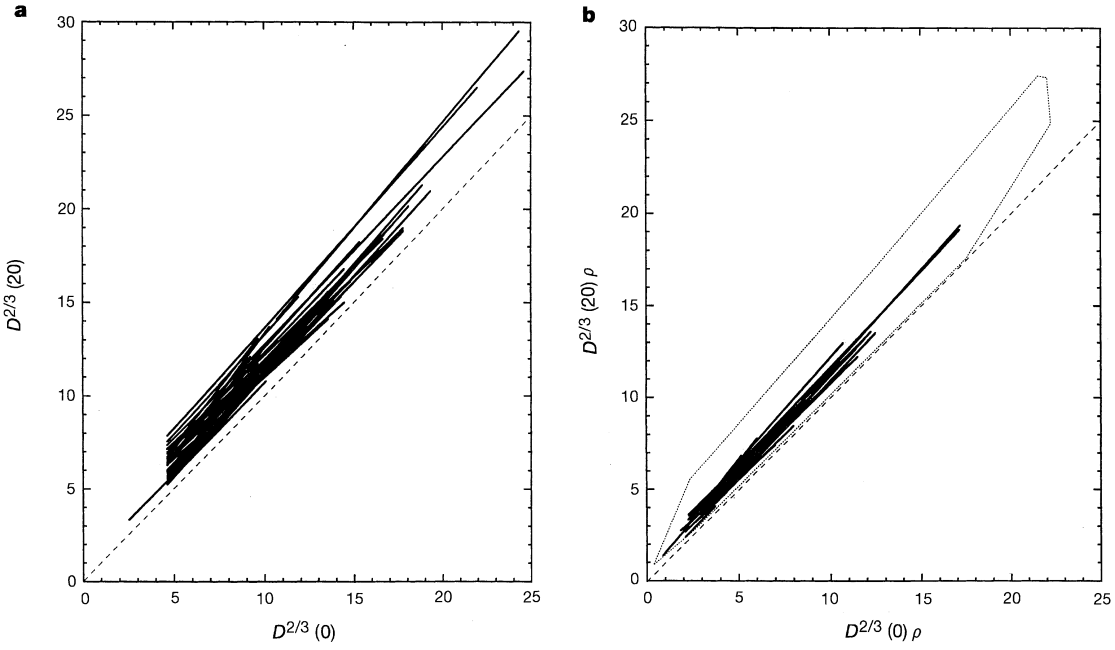

Figure 2 Growth rates of multiple species of tropical forest trees. **a**, $D^{2/3}(0)$ versus $D^{2/3}(20)$ for 45 species of dry forest trees. If production rate scales as $M^{3/4}$ (equation (2)), a slope of 1 (equation (5)) should be obtained. Note that all species have slopes that are essentially indistinguishable from 1, represented by the dashed line of unity. Statistics for each species are reported in Table 1. **b**, Weighting each species production $D(20)^{2/3} = A_1 + D(0)^{2/3}$ by wood density, ρ, collapses its production relationship onto a common line with unit slope and intercept A (see equation (6)). The dotted box shows the much greater range of variation represented in Fig. 2a. The coefficient of variation of variation for intercepts is reduced, as predicted, from 65.8 to 54.33.

Table 1 Taxonomic and Model II RMA regression statistics for production relationships $D^{2/3}(0)$ versus $D^{2/3}(20)$ for 45 species of tropical trees

Species	Family	*n*	ρ	Slope	Intercept	r^2	95%
Agonandra macrocarpa L.O. Wms.	Opiliaceae	19	0.74	0.978	1.484	0.874	0.759–1.196
Albizzia adinocephala (Donn.Sm.) Britt. & Rose	Fabaceae	13	–	1.059	1.521	0.685	0.664–1.453
Allophyllus occidentalis (Sw.) Radlk.	Sapindaceae	7	–	0.987	0.840	0.820	0.505–1.470
Annona reticulata L.	Annonaceae	13	0.57	0.981	1.046	0.826	0.709–1.252
Astronium graveolens Jacq.	Anacardiaceae	73	0.74	0.994	1.127	0.903	0.921–1.067
Ateleia herbert-smithii Pittier	Fabaceae	24	–	1.008	1.854	0.935	0.894–1.121
Bombacopsis quinata (Jacq.) Dugand	Bombaceae	23	0.47	1.000	2.327	0.649	0.731–1.269
Bursera simaruba (L.) Sarg.	Burseraceae	191	0.495	0.935	2.838	0.812	0.877–1.000
Calycophyllum candidissimum (Vahl.) DC.	Rubiaceae	83	0.685	0.926	2.175	0.887	0.857–1.000
Capparis indica (L.) Fawc. & Druce	Capparidaceae	19	–	1.090	0.485	0.815	0.850–1.329
Cecropia peltata L.	Moraceae	12	0.30	1.173	1.307	0.549	0.589–1.756
Cedrela odorata L.	Meliaceae	38	0.49	1.002	2.714	0.883	0.887–1.118
Chomelia spinosa Jacq.	Rubiaceae	65	0.72	1.121	0.174	0.672	0.959–1.282
Cochlospermum vitifolium (Wild.) Spreng.	Cochlospermaceae	90	0.19	1.067	2.607	0.600	0.859–1.280
Cordia alliodora (R. & P.) Oken	Boragenaceae	43	0.651	1.245	0.499	0.273	0.910–1.580
Cordia panamensis Riley	Boragenaceae	32	–	0.978	1.235	0.727	0.787–1.169
Dilodendron costaricense (Radlk.) Gentry & Steyerm.	Sapindaceae	10	–	0.944	2.210	0.887	0.685–1.202
Enterolobium cyclocarpum (Jacq.) Griseb.	Fabaceae	13	0.44	1.131	2.024	0.663	0.695–1.566
Exostema mexicanum A. Gray	Rubiaceae	126	–	0.952	2.248	0.703	0.860–1.044
Guarea glabra Vahl.	Meliaceae	7	–	0.958	0.806	0.980	0.802–1.114
Guazuma ulmifolia Lam.	Sterculiaceae	233	0.635	1.073	1.033	0.768	1.000–1.140
Guettarda macrosperma Don. Sm.	Rubiaceae	43	–	0.882	3.053	0.846	0.772–0.991
Hemiangium excelsum (HBK.) Ac.Smith	Hippocrateaceae	61	–	1.121	0.109	0.713	0.965–1.280
Licania arborea Seem.	Chrysobalanaceae	33	0.675	1.086	0.507	0.966	1.000–1.160
Lonchocarpus costaricensis (Con.Sm.) Pitt	Fabaceae	11	0.62	1.109	0.710	0.858	0.794–1.424
Luehea speciosa Wild.	Tiliaceae	381	0.91	1.100	0.589	0.902	1.060–1.131
Machaerium biovulatum Mecheli	Fabaceae	21	0.90	1.028	0.828	0.826	0.822–1.234
Maclura tinctoria (L.) Don	Moraceae	81	0.485	1.060	1.983	0.753	0.943–1.180
Manilkara chicle (Pittier) Gilly	Sapotaceae	37	0.45	0.979	1.411	0.931	0.890–1.067
Myrospermum frutescens Jacq.	Fabaceae	11	0.705	0.998	1.876	0.903	0.763–1.233
Ocotea veraguensis (Meisn.) Mez	Lauraceae	31	–	1.094	0.171	0.742	0.883–1.300
Pisonia macranthocarpa Donn.Smith	Nyctangaceae	28	–	1.009	0.637	0.857	0.855–1.163
Pithecellobium saman (Jacq.) Benth	Fabaceae	11	0.645	1.056	0.544	0.919	0.829–1.283
Rehdera trinervis (Blake) Mold.	Verbenaceae	17	–	0.850	2.691	0.913	0.713–0.988
Sapium thelocarpum Schm. & Pitt.	Euphorbiaceae	34	0.50	1.296	0.383	0.668	1.022–1.570
Schoepfia schreberi J.F. Gemel.	Olacaceae	17	0.70	1.111	0.485	0.785	0.828–1.395
Sciadodendron excelsum Griseb.	Ariliaceae	20	–	1.074	2.882	0.715	0.790–1.359
Sideroxylon capiri (A.DC.) Pitter	Sapotaceae	10	0.67	1.050	1.142	0.901	0.780–1.320
Simarouba glauca DC.	Simaroubaceae	20	0.68	1.028	1.100	0.932	0.900–1.564
Spondias mombin L.	Anacardiaceae	144	0.395	0.906	2.772	0.723	0.827–0.985
Tabebuea ochracea Standl.	Bignoniaceae	55	0.975	1.050	0.760	0.852	0.935–1.156
Tabebuea rosea (Bertol.) DC.	Bignoniaceae	12	0.75	1.060	0.778	0.953	0.897–1.219
Trichilia americana (Sesse & Mocino) T.D. Penn.	Meliaceae	20	0.44	1.004	1.741	0.778	0.770–1.239
Trichilia cuneata Radlk.	Meliaceae	39	–	0.877	2.240	0.725	0.724–1.030
Zuelania guidonia (Sw.) Britton & Millsp.	Flacortiaceae	12	–	1.292	–0.335	0.860	0.951–1.633

Note that 95% confidence intervals for essentially all species include the predicted slope of 1 indicating that production $\propto M^{3/4}$.

the optimal life history yield the approximate rule

$$E_\alpha \approx \frac{(1.3)\rho^{3/4} M_\alpha^{1/4}}{C_G C_B} \qquad (1)$$

for the average adult lifespan, E_α, is related to size at maturation, M_α. Equation (1) states that between species with similar M_α, E_α is proportional to $\rho^{3/4}$. If wood density is constant, this also implies that E_α is proportional to $M_\alpha^{1/4}$. Although we are not aware of any data sets precise enough to test this prediction, qualitative support is provided by several studies showing a generally positive relationship between wood density, lifespan and age to reproduction[4,11,19,22–24]. In the future, one could relax the assumption $\lambda = 1$ and explore the general case.

The framework developed above highlights the central roles of allometric scaling and wood density in the life histories of trees. The tropical tree species studied here varied from fast-growing disturbance specialists with low-density wood and short life spans to slow growing emergent trees with dense wood and long life spans. Despite all of this variation, production scaled as $M^{3/4}$, the same as in animals[1,14]. Although all of the tree species produced new biomass at nearly the same rates (Fig. 2b), differences in wood density resulted in substantial differences in growth rates as measured as change in basal diameter (Fig. 2a). Wood density is frequently cited as being a 'principal determinant' of life history variation in woody plants[11,19,22–26]. It is correlated with stem water storage and transport capacity, resistance to decay and leaf characteristics such as toughness and deciduousness[4,11,1922–26]. Although the size of trees powerfully constrains rates of carbon fixation, differences in carbon allocation strategies facilitate the coexistence of multiple species in tropical forests owing to variation in growth rate, lifespan and reproductive effort[10].

We have shown that a general allometric framework incorporating the specifics of vascular transport and allocation can account for numerous features of biological diversity[14–16]. Because of the availability of data to evaluate the model, we have focused on scaling of growth and reproduction in trees; however, the model could easily be modified for plants with different growth forms (herbs) and life histories (monocarpy). Many details of plant anatomy, physiology, and ecology (for example, water and nutrient availability, plant density) can be incorporated into the allometric coefficients (the *C*s) to link pattern and process across multiple scales of biological organization. Interspecific variation in allocation to roots or defences should also be reflected in the *C* values. Production is ultimately limited by the physical and biological constraints that limit transportation through the vascular system. However, species differ in how they allocate production. These differences in rates of growth, life span, time until reproduction, wood density and other variables can be mechanistically linked to a general allometric framework of allocation. More importantly, this framework shows how size-dependent variation in life-history strategies can be derived from a set of general allometric principles. □

Methods

Study area

Measurements of diameters at breast height (dbh) of trees were recorded within a permanently marked study plot of seasonally dry tropical forest (10° 45′ N, 85° 30′ W)

within Sector Santa Rosa, Area de Conservacion, Guanacaste (ACG), of northwest Costa Rica[27]. In 1976, all stems ≥3 cm dbh were mapped within a continuous 680 m × 240 m (16.32 Ha) area of forest[20] by S. P. Hubbell. Using an identical mapping protocol, a second remap of the San Emilio forest was completed between 1995 and 1996. In total, 46,833 individuals have been surveyed, 26,960 in 1976 and 19,873 in 1996. Together, the two surveys document 20 yr of growth and population change for about 150 species. The plot is composed of secondary growth forest and is heterogeneous with respect to age, topography and degree of deciduousness.

Calculation of individual tree growth

In 1976, most trees greater than 10 cm dbh were tagged with aluminum tree markers and given a unique identification number. Because few smaller individuals were given aluminum tags in 1976, tree growth was usually followed only for those trees greater than 10 cm dbh. Growth was calculated by monitoring changes in dbh for each individual. To ensure an accurate estimate of growth, a species was included only if a minimum representation of seven individuals had initial stem diameters ≥10 cm, and the diameter range of all individuals ≥20 cm. As the minimum diameter cut off for individuals was 10 cm, this imposed a minimum size range of 30 cm. Only individuals experiencing positive growth in the 20-year period were used for the calculation of allometric equations. In some cases, individuals experienced no change or even a decrease in diameter over time. This was usually due to partial death, loss of the main trunk or measuring errors. The 45 species meeting the above criteria are listed in Table 1. Production equations for each species were generated by plotting $D^{2/3}(0)$ versus $D^{2/3}(20)$ on linear axes. Because dbh was measured identically in 1976 and 1996, measurement error is likely to be equally distributed across the x and y axes. For these reasons, allometric slopes were determined using Model II RMA regression[1,28,29]. Equations and statistics for each species are also reported in Table 1.

Species-specific wood density

The specific wood density, ρ, is a simple measure of the total dry mass per unit volume of wood (g cm^{-3}). The specific density of wood is closely related to mechanical properties of strength, such as elastic moduli, which describe resistance to static and impact bending, compression and tension[28]. For 29 of the 45 species reported in this study, values of specific wood density, ρ, in g cm^{-3}, were taken from the literature[24,26,30]. If more than one study reported a different value for a species, then the average value was used (Table 1).

Received 9 June; accepted 12 August 1999.

1. Charnov, E. L. *Life History Invariants: Some Explorations of Symmetry in Evolutionary Ecology* (Oxford Univ. Press, Oxford, 1993).
2. Stearns, S. C. *The Evolution of Life Histories* (Oxford Univ. Press, Oxford, 1992).
3. Richards, P. W. *The Tropical Rain Forest* 2nd edn (Cambridge Univ. Press, Cambridge, 1996).
4. Chambers, J. Q., Higuchi, N. & Schimel, J. P. Ancient trees in Amazonia. *Nature* **391,** 135–136 (1998).
5. Grime, J. P. & Hunt, R. Relative growth-rate: its range and adaptive significance in a local flora. *J. Ecology* **63,** 393–422 (1975).
6. Tilman, D. *Plant Strategies nd the Dynamics and Structure of Plant Communities* (Princeton Univ. Press, Princeton, 1988).
7. Cebran, J. & Duarte, C. M. The dependence of herbivory on growth rate in natural plant communities. *Func. Ecol.* **8,** 518–525 (1994).
8. Gleeson, S. K. & Tilman, D. Plant allocation, growth rate and successional status. *Func. Ecol.* **8,** 543–550 (1994).
9. Ricklefs, R. E. Environmental heterogeneity and plant species diversity: an hypothesis. *Am. Nat.* **111,** 376–381 (1977).
10. Grubb, P. J. The maintenance of species diversity in plant communities: the importance of the regeneration niche. *Biol. Rev.* **52,** 107–145 (1977).
11. Denslow, J. S. Gap partitioning among tropical rain forest trees. *Biotropica* (Suppl.), **12**, 47–55 (1980).
12. Williamson, G. B. Gradients in wood specific gravity of trees. *Bull. Torr. Bot. Club* **111,** 51–55 (1996).
13. Hubbell, S. P. *et al.* Light-gap disturbances, recruitment limitation, and tree diversity in a neotropical forest. *Science* **283,** 554–557 (1999).
14. West, G. B., Brown, J. H. & Enquist, B. J. A general model for the origin of allometric scaling laws in biology. *Science* **276,** 122–126 (1997).
15. Enquist, B. J., Brown, J. H. & West, G. B. Allometric scaling of plant energetics and population density. *Nature* **395,** 163–165 (1998).
16. West, G. B., Brown, J. H. & Enquist, B J. A general model for the structure and allometry of plant vascular systems. *Nature* **400,** 664–667 (1999).
17. Peters, R. H. *et al*. The allometry of the weight of fruit on trees and shrubs in Barbados. *Oecologia* **74,** 612–616 (1988).
18. Niklas, K. The allometry of plant reproductive biomass and stem diameter. *Am. J. Bot.* **80,** 461–467 (1993).
19. Thomas, S. C. Reproductive allometry in Malaysian rain forest trees: biomechanics verses optimal allocation. *Evol. Ecol.* **10,** 517–530 (1996).
20. Stevens, G. C. Lianas as structural parasites: the *Bursera simaruba* example. *Ecol.* **68**, 77–81 (1987).
21. Whittaker, R. H. & Woodwell, G. M. Dimension and production relations of trees and shrubs in the Brookhaven Forest, New York. *Ecology* **56,** 1–25 (1968).
22. Smith, D. W. & Tumey, P. R. Specific density and caloric value of the trunk wood of white birch, black cherry, and sugar maple and their relationship to forest succession. *Can. J. For. Res.* **12,** 186–190 (1982).
23. Augspurger, C. K. Seed dispersal of the tropical tree *Platyposdium elegans* and the escape of its seedlings from fungal pathogens. *J. Ecol.* **71,** 759–771 (1983).
24. Borchert, R. Soil and stem water storage determine phenology and distribution of Dry Tropical forest trees. *Ecology* **75,** 1437–1449 (1994).
25. Sobrado, M. A. Aspects of tissue water relations of evergreen and seasonal changes in leaf water potential components of evergreen and deciduous species coexisting in tropical forests. *Oecologia* **68,** 413–416 (1986).
26. Fearnside, P. M. Wood density for estimating forest biomass in Brazilian Amazonia. *For. Ecol. Manage.* **90,** 59–87 (1997).
27. Janzen, D. H. *Guanacaste National Park: Tropical Education, and Cultural Restoration* (Editorial Univ. Estatal a Distanca, San Jose, 1986).
28. Niklas, K. J. *Plant Allometry: The Scaling of Form and Process* (Univ. Chicago Press, Chicago, 1994).
29. Harvey, P. H. & Pagel, M. D. *The Comparative Method in Evolutionary Biology* (Oxford Univ. Press, Oxford, 1991).
30. Malavassi, I. C. *Maderas de Costa Rica: 150 Especies Forestales* (Univ. de Costa Rica, San Jose, 1998).

Acknowledgements

We thank R. J. Whittaker, G. C. Stevens, D. H. Janzen, J. J. Sullivan, L. Brown, C. A. F. Enquist, A. Masis and the A.C.G. for comments and help with data collection. B.J.E. was supported by a NSF postdoctoral fellowship, G.B.W. by the US Department of Energy and the NSF, E.L.C. by a MacArthur fellowship and J.H.B. by a University of New Mexico Faculty Research Semester. B.J.E., G.B.W. and J.H.B. were also supported by the Thaw Charitable Trust.

Correspondence and requests for materials should be addressed to B.J.E. (e-mail: enquist@nceas.ucsb.edu).

Optimizing the success of random searches

G. M. Viswanathan*†‡, Sergey V. Buldyrev*, Shlomo Havlin*§, M. G. E. da Luz‖¶, E. P. Raposo‖# & H. Eugene Stanley*

* *Center for Polymer Studies and Department of Physics, Boston University, Boston, Massachusetts 02215, USA*
† *International Center for Complex Systems and Departamento de Física Teórica e Experimental, Universidade Federal do Rio Grande do Norte, 59072-970, Natal-RN, Brazil*
‡ *Departamento de Física, Universidade Federal de Alagoas, 57072-970, Maceió-AL, Brazil*
§ *Gonda-Goldschmied Center and Department of Physics, Bar Ilan University, Ramat Gan, Israel*
‖ *Lyman Laboratory of Physics, Harvard University, Cambridge, Massachusetts 02138, USA*
¶ *Departamento de Física, Universidade Federal do Paraná, 81531-970, Curitiba-PR, Brazil*
# *Laboratório de Física Teórica e Computacional, Departamento de Física, Universidade Federal de Pernambuco, 50670-901, Recife-PE, Brazil*

We address the general question of what is the best statistical strategy to adapt in order to search efficiently for randomly located objects ('target sites'). It is often assumed in foraging theory that the flight lengths of a forager have a characteristic scale: from this assumption gaussian, Rayleigh and other classical distributions with well-defined variances have arisen. However, such theories cannot explain the long-tailed power-law distributions[1,2] of flight lengths or flight times[3–6] that are observed experimentally. Here we study how the search efficiency depends on the probability distribution of flight lengths taken by a forager that can detect target sites only in its limited vicinity. We show that, when the target sites are sparse and can be visited any number of times, an inverse square power-law distribution of flight lengths, corresponding to Lévy flight motion, is an optimal strategy. We test the theory by analysing experimental foraging data on selected insect, mammal and bird species, and find that they are consistent with the predicted inverse square power-law distributions.

Lévy flights are characterized by a distribution function

$$P(l_j) \sim l_j^{-\mu} \qquad (1)$$

with $1 < \mu \leq 3$, where l_j is the flight length. The gaussian is the stable distribution for the special case $\mu \geq 3$ owing to the central-limit theorem, while values $\mu \leq 1$ do not correspond to probability distributions that can be normalized[2]. This generalization, equation (1), introduces a natural parameter μ such that we essentially have a